Published in final edited form as:
Nature. 2021 November 01; 599(7884): 273–277. doi:10.1038/s41586-021-04037-6.

Antagonistic cell surface and intracellular auxin signalling regulate plasma membrane H⁺-fluxes for root growth

Lanxin Li[#1], **Inge Verstraeten**[#1], **Mark Roosjen**[2], **Koji Takahashi**[3,4], **Lesia Rodriguez**[1], **Jack Merrin**[1], **Jian Chen**[5,6], **Lana Shabala**[7], **Wouter Smet**[5,6], **Hong Ren**[8], **Steffen Vanneste**[5,9,10], **Sergey Shabala**[7,11], **Bert De Rybel**[5,6], **Dolf Weijers**[2], **Toshinori Kinoshita**[3,4], **William M. Gray**[8], **Jiří Friml**[1]

[1]Institute of Science and Technology (IST) Austria – 3400 Klosterneuburg (Austria)

[2]Department of Agrotechnology and Food Sciences, Laboratory of Biochemistry, Wageningen University – 6708 WE Wageningen (the Netherlands)

[3]Institute of Transformative Bio-Molecules, Nagoya University, Division of Biological Science – 464-8602 Chikusa Nagoya (Japan)

[4]Graduate School of Science, Nagoya University – 464-8602 Chikusa Nagoya (Japan)

[5]Ghent University, Department of Plant Biotechnology and Bioinformatics – 9052 Gent (Belgium)

[6]VIB Center for Plant Systems Biology – 9052 Gent (Belgium)

[7]Tasmanian Institute of Agriculture, College of Science and Engineering, University of Tasmania – Hobart (Australia)

[8]Department of Plant & Microbial Biology, University of Minnesota – MN-55108, St. Paul (United States)

[9]Lab of Plant Growth Analysis, Ghent University Global Campus – Incheon 21985 (Republic of Korea)

[10]Department of Plants and Crops - HortiCell, Ghent University – 9000 Gent (Belgium)

[11]International Research Centre for Environmental Membrane Biology, Foshan University – 528000 Foshan (China)

Correspondence to: Jiří Friml.

[*]Correspondence to: Correspondence and requests for materials should be addressed to J.F. jiri.friml@ist.ac.at .

Author contributions.

L.L., I.V. and J.F. conceived and designed the experiments. L.L. and I.V. carried out most of the experiments and analysis. M.R. and D.W. performed the phospho-proteomics analysis and TIR1 and AFB1 IP-MS/MS. I.V., W.S. and B.D.R. performed TMK1 IP-MS/MS experiments and statistical analysis. MS/MS analysis was performed by the VIB Proteomics Core. L.S. and S.S. performed MIFE experiments. K.T. and T.K. did the ATP hydrolysis assays. J.C. and S.V. created and shared the *AtTAS1c-AHA* lines. L.R. and L.L. created transgenic lines and crosses. H.R. and W.M.G. conducted leaf wilting phenotype analysis, western blot of *tmk1,4*, shared plasmids, seeds materials and contributed to discussion of the results. J.M. and L.L. modified the microfluidic chip. L.L, I.V. and J.F. wrote the manuscript.

Competing interests.

The authors declare no competing interests.

Additional information

The main data supporting the findings of this study are available within the paper and its Extended Information. Additional data are available from the corresponding authors upon reasonable request.

Europe PMC Funders Author Manuscripts

# These authors contributed equally to this work.

Abstract

Growth regulation tailors plant development to its environment. A showcase is growth adaptation to gravity, where shoots bend up and roots down. This paradox is based on different responses to the phytohormone auxin, which promotes cell expansion in shoots, while inhibiting it in roots via a yet unknown cellular mechanism. Here, by combining microfluidics, live imaging, genetic engineering and phospho-proteomics in *Arabidopsis thaliana*, we reveal how auxin inhibits root growth. We show that auxin activates two distinct, antagonistically acting signalling pathways that converge on the rapid regulation of the apoplastic pH, which is the direct growth-determining mechanism. Cell surface-based TRANSMEMBRANE KINASE 1 (TMK1) interacts with and mediates phosphorylation and activation of plasma membrane H^+-ATPases for apoplast acidification, while intracellular TIR1/AFB-mediated signalling triggers net cellular H^+-influx, causing apoplast alkalinisation. The simultaneous activation of these two counteracting mechanisms poises the root for a rapid, fine-tuned growth modulation to subtle changes in the environment.

Auxin, as a major growth regulator in plants, acts oppositely in shoots and roots. In shoots, it promotes cell elongation by activating H^+-pumps to acidify the apoplast [1] in agreement with the classical Acid Growth Theory, which postulates that low apoplastic pH promotes growth [2–4] . This relatively slow process relies on the canonical/intracellular TIR1/AFB receptors-mediated pathway of transcriptional regulation [5–7] . In many species including the model Arabidopsis, however, auxin inhibits growth in roots [8] by an unclear cellular mechanism. This contrasting response to the same signal is the basis for the positive versus negative bending of roots and shoots in response to gravity and light. The inhibitory auxin effect in roots is very rapid, but also involves TIR1/AFB receptors [9] . The timing indicates the existence of a rapid, non-transcriptional branch of this pathway [9] , nonetheless with unclear downstream molecular, cellular and physiological mechanisms. Besides intracellular TIR1/AFB auxin signalling, a cell surface-based pathway mediated by TRANSMEMBRANE KINASE 1 (TMK1) has been shown to regulate differential growth in the apical hook [10] , while its contribution to a general growth regulation, remains unclear. Hence, the auxin signalling mechanism and the downstream cellular mechanisms for regulating root growth remain elusive.

In this study, we revealed simultaneous antagonistic activities of TIR1/AFB intracellular and TMK1-based cell surface auxin signalling converging on regulation of apoplastic pH, which we identified as the key cellular mechanism allowing immediate and sensitive root growth regulation.

Auxin-induced root growth inhibition correlates with a rapid increase in apoplastic pH

Auxin rapidly and non-transcriptionally inhibits root growth through TIR1/AFB auxin signalling [9] . Although several processes, including cortical microtubule (CMT) reorientation [11,12] , vacuolar fragmentation [13] and apoplastic pH changes [14–16] are

implicated, the causal mechanism mediating rapid auxin inhibition of root growth remains unidentified.

The microfluidic vRootchip [9] setup in combination with vertical confocal microscopy [17] allowed us to critically re-evaluate the contributions of these processes by comparing their kinetics. Growth inhibition was observed within 30 seconds after 10 nM of the natural auxin indole-3-acetic acid (IAA) [9] . Using the microtubule plus-end marker *pEB1b::EB1b-GFP*, we observed that even using 100 nM IAA, less than 5% of the CMT in elongating epidermal cells reoriented after 1 minute (Extended Data Fig. 1a-b). Furthermore, inhibition of CMT dynamics by taxol treatment blocked auxin-mediated CMT reorientation (Extended Data Fig. 1c-d), but had no effect on auxin-mediated growth inhibition (Extended Data Fig. 1e). We visualized vacuolar morphology using tonoplast marker *pSYP22::SYP22-YFP*. By live imaging the same cells, we could not detect obvious changes in vacuolar morphology even after 30 minutes of 100 nM IAA treatment (Extended Data Fig. 1f), when root growth was already strongly inhibited. These results show that both CMT reorientation and vacuole constriction occur well after the rapid auxin-mediated growth inhibition, arguing against their involvement in this process.

To evaluate the kinetics of apoplastic pH changes, we applied a membrane-impermeable ratiometric pH indicator: 8-hydroxypyrene-1,3,6-trisulfonic acid (HPTS) [14] and imaged apoplastic pH in elongating epidermis cells while simultaneously tracking root tip growth in the vRootchip. We detected a gradient in the apoplastic pH, decreasing from transition to elongation zone, in root epidermal cells (Extended Data Fig. 1g). Regardless of their position, all cells showed a strong apoplastic pH increase within 30 seconds of 5 nM IAA treatment (Fig. 1a, b and Extended Data Fig. 1g). This auxin-mediated alkalinisation was observed at the same time as root growth inhibition (Fig. 1b). The pH increase was very robust as we also detected alkalinisation of the external medium along the root tip surface (Extended Data Fig. 1h). In a complementary approach, we analysed the cytosolic pH by using the PM-Cyto reporter [18] . The cytosolic pH adjacent to the PM decreased within 30 seconds of 5 nM IAA treatment (Fig. 1c). The concomitant apoplastic pH increase and intracellular decrease in elongating root epidermal cells suggest that auxin causes a H^+-influx into the cell. This notion was confirmed in direct experiments using non-invasive ion microelectrodes monitoring the net H^+-exchange across the PM of root elongating epidermis cells (Extended Data Fig. 1i).

Overall, auxin triggers rapid apoplast alkalinisation by increasing the net H^+-flux into cells. Strong spatial and temporal correlation with auxin-mediated root growth inhibition suggests that apoplast alkalinisation may be the key cellular mechanism, by which auxin rapidly inhibits root growth.

Apoplastic pH is causative for rapid root growth regulation

To investigate the causal relationship between apoplast alkalinisation and root growth inhibition, we manipulated the apoplastic pH by changing the pH of the medium and monitoring the impact on root growth using the vRootchip. Indeed, pH manipulation of the medium had a rapid impact on the root apoplastic pH (Extended Data Fig. 1j-k).

Replacement of the standard medium at pH 5.8 by a more alkaline (pH 6.15) medium caused instant reduction of root growth; the growth rate restored rapidly after washout with the original pH 5.8 medium (Fig. 1d, e). Gradual alkalinisation of the medium resulted in gradual root growth inhibition (Extended Data Fig. 1l). On the other hand, replacing the alkaline medium by more acidic pH 5.1 medium increased root growth instantly and washout restored the original growth rate (Fig. 1f, g).

Thus, exogenous manipulation of apoplastic pH has an immediate and reversible effect on root growth, with alkaline pH inhibiting and acidic pH promoting growth. This resembles the root growth inhibition effects of auxin in both speed and reversibility and strongly supports that auxin-induced apoplast alkalinisation is the key downstream cellular mechanism for rapid root growth inhibition.

Auxin rapidly phosphorylates and activates plasma membrane H^+-ATPases in the root

The auxin effect on apoplast alkalinisation occurs within seconds, thus being too fast to involve transcriptional regulation. To gain insights into the underlying mechanism, we mined recent datasets from Mass Spectroscopy (MS)-aided phospho-proteomics in *Arabidopsis* root tips treated for 2 minutes with 100 nM IAA (Han et al., manuscript in preparation). Among the top differentially phosphorylated targets were two Plasma Membrane (PM) H^+-ATPases encoded by AT2G18960 (AHA1) and AT4G30190 (AHA2). Multiple putative phosphorylation sites were identified in the auto-inhibitory C-terminal region as being regulated by auxin, potentially leading to both activation and deactivation of H^+-pump activity [19,20] (Fig. 2a and Extended Data Table 1). This suggested that auxin may regulate H^+-pump activity in roots via phosphorylation, providing a plausible mechanism for the observed rapid auxin effect on apoplastic pH.

To test whether and how auxin changes the activity of PM H^+-ATPases in roots, we performed an ATP hydrolysis assay measuring the hydrolytic release of inorganic phosphate from the ATP, which has been shown to correlate with the activity of the H^+-ATPases and with the H^+-extrusion [21,22] . After 1 hour 100 nM IAA treatment, we detected increased ATP hydrolysis activity in root protein extracts (Fig. 2b), similarly as observed in shoots following auxin treatment (Lin et al., submitted). This supports the notion that auxin activates H^+-pumps also in root cells, which should lead to apoplast acidification contrasting with the observed alkalinisation (see Fig. 1b).

Hereafter, we reanalysed the phospho-proteomics data specifically for the phosphorylation of Thr^{947} in AHA2, a known activation site [23,24] . Thr^{947} was significantly more phosphorylated after IAA treatment (Fig. 2c), suggesting that auxin activates AHAs in the root by stimulating this phosphorylation. To confirm the phosphorylation state of AHA2, we used antibodies that specifically recognize the catalytic domain of AHA2 and phosphorylated Thr^{947}. We pre-treated seedlings with 50 μM of the auxin biosynthesis inhibitor kynurenine for 24 hours, followed by 10 nM IAA treatment and harvested roots at given time points. At such low concentration, IAA strongly induced phosphorylation of Thr^{947} of AHA2 within 10-20 minutes and additionally led to an increase of AHA2 protein

levels at later time points (Fig. 2d). Thus, auxin mediates AHA2 phosphorylation leading to its activation.

Our results show that, consistently with previous findings in shoots [7,22], auxin rapidly induces AHA phosphorylation leading to H^+-pump activation in the root. This, however, should lead to apoplast acidification and not the observed auxin-induced apoplast alkalinisation (see Fig. 1b) suggesting that in roots H^+-pump activation may act antagonistically, presumably as a negative feed-back to auxin-mediated apoplast alkalinisation.

H^+-ATPases activation counteracts auxin-mediated apoplast alkalinisation and growth inhibition

To better understand the role of H^+-pump activation during auxin-mediated root growth inhibition, we used the fungal toxin Fusicoccin (FC). FC stabilizes binding of 14-3-3 proteins to H^+-ATPases, thus rapidly and specifically activating them [23,25,26], without otherwise affecting auxin signalling (Extended Data Fig. 2a). This allowed us to dissect the effects of auxin and H^+-ATPase activation on pH and growth simultaneously. FC caused rapid apoplast acidification and promoted growth in roots (Extended Data Fig. 2b, c), opposite to the auxin effect. When FC and IAA were applied simultaneously, we observed an intermediate outcome on apoplastic pH and root growth proportional to the ratio of auxin versus FC (Fig. 2e, f and Extended Data Fig. 2f, g). Similar observations were made when FC and IAA were added sequentially (Extended Data Fig. 2b-e). These observations suggest that FC-mediated H^+-ATPase activation and IAA-mediated apoplast alkalinisation act antagonistically during apoplastic pH and root growth regulation.

To test this notion genetically, we analysed auxin response of loss- and gain-of-function *aha* mutants. Single *aha1* and *aha2* mutants have no consistent root phenotypic defects, when grown on auxin (Extended Data Fig. 2h), while the double mutant is embryo-lethal [27]. To overcome redundancy within the AHA family and test for AHA function specifically in cells where root growth is controlled, we used a synthetic trans-acting siRNA [28] targeting *AHA1/2/7/11* (*AtTAS1c-AHA*), expressed from the *PIN2* promoter in the outer root tissues [29]. Expression of all four *AHAs* was verifiably downregulated in both independent transgenic lines (Extended Data Fig. 2i). Both *AtTAS1c-AHA* lines were hypersensitive to auxin in terms of apoplast alkalinisation (Fig. 2g) and root growth inhibition (Fig. 2i). In contrast, constitutive activation of AHA1 in the *ost2-3D* mutants [30] resulted in decreased auxin sensitivity of apoplastic pH (Fig. 2h) and root growth (Fig. 2i). These *aha* mutant phenotypes further confirm that auxin-mediated H^+-ATPase activation antagonizes auxin-induced apoplast alkalinisation in the root.

These observations show that H^+-pump activation in roots acts against the observed auxin-mediated apoplast alkalinisation. The auxin effect on root growth is thus the net result of auxin-induced AHA activation, which presumably acts as negative feed-back against the more dominant auxin-mediated alkalinisation.

TMK1 interacts with H+-ATPases

To gain insights into the mechanisms, by which auxin signalling regulates apoplastic pH, we performed co-immunoprecipitation pull-down assays followed by MS-assisted identification of proteins associated with either the intracellular TIR1/AFB1 receptor or the cell surface TMK1 Leucine-rich repeat receptor-like kinase [31] . For TIR1 and AFB1 this approach did not reveal any components that have yet been linked to control of H^+-transport (Extended Data Fig. 3a and Extended Data Table 2). For TMK1, although enrichment was not strong and the identified peptides did not allow discriminating between the two proteins, we found peptides of AHA1/AHA2 among the top enriched associated peptides for TMK1 (Extended Data Fig. 3b and Extended Data Table 3).

To verify the interaction between AHAs and TMK1, we performed Co-IP assays from transgenic *pTMK1::TMK1-FLAG* (Fig. 3a), *pAHA2::AHA2-GFP* (Fig. 3b) and *pTMK1-TMK1-GFP* roots (Extended Data Fig. 3c). In all pulldowns with TMK1-expressing plants, we detected associated AHA2 and reciprocally from the AHA2-GFP pulldowns, we detected TMK1, confirming interaction between TMK1 and AHA2. IAA treatment had no effect on the interaction, but AHA2 phosphorylation was increased (Fig. 3a, b and Extended Data Fig. 3c). Additionally, we confirmed the interaction *in vivo* by bimolecular fluorescent complementation (BiFC) in tobacco leaves co-transformed with TMK1 and AHA2 (Fig. 3c and Extended Data Fig. 3d).

These observations show that TMK1, a presumable component of cell surface auxin signalling, interacts with the PM H^+-ATPase AHA2.

TMK1 activity mediates auxin effect on H+-ATPases phosphorylation and activation

To test the role of TMK1 in H^+-ATPase phosphorylation, we performed phospho-proteomic analysis in roots of *tmk1-1* compared to WT, and detected strong hypophosphorylation of AHAs in the *tmk1-1* (Fig. 3d and Extended Data Table 1). This stipulates that TMK1 is involved in H^+-ATPases phosphorylation.

To further confirm this notion, we cloned *p35S::TMK1-HA* and two kinase-dead versions with mutations in the ATP binding site, in which K^{616} is exchanged to either E or R ($TMK1^{K616E}$ or $TMK1^{K616R}$). Transient overexpression of the wild type (WT), but not the kinase-dead TMK1 constructs in tobacco resulted in rapid wilting of the leaves (Extended Data Fig. 3e), an effect consistent with PM H^+-ATPases activation [32] . To test this directly in *Arabidopsis* roots, we generated dexamethasone (DEX)-inducible TMK1 gain-of-function lines and assessed the phosphorylation status of AHA2. In the root extract expressing $TMK1^{K616R}$, no phosphorylation of AHA^{Thr947} was observed after 100 nM IAA treatment compared to $TMK1^{WT}$ (Extended Data Fig. 3f).

Next, we analysed different *tmk* loss-of-function mutants. We detected less auxin-induced AHA phosphorylation in *tmk1-1* single and *tmk1-1, tmk3-1* (*tmk1,3)* double mutants compared to WT (Fig. 3e, f and Extended Data Fig. 3g, h). As double *tmk1-1, tmk4-1*

(*tmk1,4)* plants were very stunted, protein extracts were prepared from full seedlings and less endogenously phosphorylated AHA2 was detected (Fig. 3g). We also assessed the H^+-ATPase activity by the ATP hydrolysis assay. We detected auxin-induced increase of H^+-ATPase activity in WT but not in the *tmk1-1*, *tmk4-1* and *tmk1,4* roots (Fig. 3h).

In summary, these independent approaches show that active TMK1 kinase is required for the auxin-mediated phosphorylation and activation of H^+-ATPases in roots.

TIR1/AFB and TMK1 signalling converge antagonistically on apoplastic pH and growth regulation

Our results show that TMK1 interacts with, and mediates the phosphorylation and activation of PM H^+-ATPases (see Fig. 3), which results in apoplast acidification (see Fig. 2). How can we reconcile this with the observed auxin-mediated apoplast alkalinisation leading to growth inhibition (see Fig. 1)?

Previously, it was proposed that the auxin influx transporter AUXIN RESISTANT1 (AUX1) and the intracellular TIR1/AFB auxin receptors mediate auxin-induced membrane depolarisation associated with changes in H^+-fluxes across the PM [15,33] . Therefore, we set out to assess the interplay of these components with TMK1 action in regulation of apoplastic pH. First, we used *aux1-100* mutants defective in the AUXIN RESISTANT 1 (AUX1), which mediates cellular uptake of IAA and, in particular, of the synthetic auxin analogue 2,4-dichlorophenoxyacetic acid (2,4-D) [34] . Consistently with previous reports [9] , *aux1-100* roots were less sensitive to 5 nM IAA in the vRootchip (Extended Data Fig. 4a, b) or to 0.1 μM 2,4-D (Extended Data Fig. 4c, d) in the steady-state conditions, both for the apoplastic pH and the root growth inhibition suggesting intracellular auxin perception is required for auxin-mediated apoplast alkalinisation.

Given that intracellular TIR1/AFB receptors mediate auxin-mediated growth inhibition [9] , we evaluated apoplastic pH in parallel to growth in the *tir1-1, afb2-1, afb3-1* (*tir triple*) mutant. The *tir triple* roots were resistant to 5 nM IAA in both apoplast alkalinisation and growth inhibition (Fig. 4a and Extended Data Fig. 4e). As a pharmacological alternative, we applied PEO-IAA, which acts as an anti-auxin and blocks downstream signalling following binding to TIR1/AFB receptors [35] . Simultaneous addition of 10 μM PEO-IAA and 5 nM IAA prevented apoplast alkalinisation and growth inhibition (Extended Data Fig. 4f, g). Both approaches further corroborate the involvement of the TIR1/AFB auxin perception in auxin-mediated apoplast alkalinisation.

To test the TIR1/AFB requirement, definitively, we took advantage of the cvxIAA/ccvTIR1 system, in which the engineered concave (ccv) TIR1 receptor cannot interact with the natural IAA, but only with a synthetic convex (cvx) IAA analogue, thus allowing specific activation of TIR1/AFB signalling [7] . Application of 50 nM cvxIAA in the vRootchip resulted in apoplastic alkalinisation in the ccvTIR1 plants, but not in the control (Fig. 4b), confirming that specific activation of the TIR1/AFB pathway is sufficient to induce root growth inhibition [9] and apoplast alkalinisation.

These observations suggest that intracellular TIR1/AFB signalling mediates the dominant auxin effect: apoplast alkalinisation and root growth inhibition. This is then counteracted by the cell surface TMK1-mediated H^+-ATPase activation for apoplast acidification. Indeed, in the steady state, TMK1 function is redundantly required for root growth as demonstrated by shorter roots in *tmk* mutants (Fig. 4c) [36]. In response to low concentration of auxin, *tmk1*-related mutants were more sensitive (Fig. 4d), while overexpressing TMK1 (*pUBQ10::TMK1-3HA*) led to a slight auxin resistance (Extended Data Fig. 4h). This resembles the corresponding loss- and gain-of-function *aha* mutants (see Fig. 2) providing additional support for the antagonistic, growth-promoting role of TMK-mediated AHA activity.

To explore further the antagonism of TIR1/AFB and TMK1, we created double mutant *tmk1-1, tir1-1* (*tmk1,tir1)* and analysed the auxin effect on apoplastic pH and root growth. As expected, the *tmk1,tir1* mutant showed intermediate auxin sensitivity compared to the single mutants both for growth and apoplastic pH (Fig. 4e, f and Extended Data Fig. 4i, j).

Collectively, these results strongly suggest that auxin activates two antagonistically acting signalling pathways: (i) the cell surface, TMK1-mediated H^+-efflux acidifying apoplast and (ii) an intracellular TIR1/AFB-dependent apopast alkalinisation leading to the rapid growth inhibition (Fig. 4g). It seems that the TIR1/AFB-mediated apoplast alkalinisation is dominant, in particular at conditions of higher auxin after its exogenous application. But at low auxin levels, TMK1-mediated acidification becomes more apparent and fine-tunes the growth inhibition outcome.

Conclusions

Our findings provide novel insights into a long-standing question on how root growth is regulated in plants. In particular, we addresses the old mystery of opposite growth regulation in shoots and roots by the phytohormone auxin and we also clarify the downstream cellular mechanism of auxin-mediated root growth inhibition.

Auxin regulates root growth very rapidly, utilizing a non-transcriptional branch of a signalling pathway downstream of intracellular TIR1/AFB receptors [9]. This pathway mediates apoplast alkalinisation, which we show as the direct, causative cellular mechanism for root growth regulation. This finding extends the classical Acid Growth Theory proposing that low apoplastic pH promotes growth [2,3]. We demonstrate validity of this mechanism also for growth inhibition, showing that root growth rate is immediately and reversibly determined by apoplastic pH changes.

Remarkably, the auxin-mediated apoplast alkalinisation in roots does not occur through the regulation of PM H^+-ATPases as observed in shoots, where the same TIR1/AFB auxin perception mechanism leads to PM H^+-ATPases activation and apoplast acidification [5,7,22].

Instead, in roots, PM H^+-ATPases are phosphorylated and activated via the cell surface TMK1 receptor like kinase-based auxin signalling, which leads to apoplast acidification and root growth promotion. This mechanism, acting antagonistically to the more dominant TIR1/

AFB-mediated alkalinisation, constitutes a negative feed-back, presumably to fine-tune root growth to be able to rapidly respond to subtle changes of environmental stimuli.

Key remaining open questions are: (*i*) if not by PM H^+-ATPases, how does TIR1/AFB signalling mediate alkalinisation in roots? A plausible scenario would be a rapid increase in H^+-permeability across the PM, which may be mediated by TIR1/AFB-activated Ca^{2+} signalling [33] and would impact on the apoplastic pH and membrane potential. (*ii*) What is the auxin perception mechanism for the TMK1 pathway? Is it direct activation of TMK1 by auxin or through another yet to be identified associated auxin receptor?

With cell surface-based TMK1 activating H^+-pumps and intracellular TIR1/AFB signalling causing the net cellular H^+-influx, two auxin-triggered antagonistic mechanisms converge on the regulation of extracellular pH, which directly determines root growth rates. This seemingly counterproductive simultaneous 'gas and brake' action presumably poises the root tip for rapid and flexible changes of the growth rate and direction in response to numerous stimuli during the challenging task to navigate through the complex soil environments.

Methods

Plant materials and growth conditions

All *Arabidopsis thaliana* mutants and transgenic lines used are in Columbia-0 (Col-0) background. The *pEB1b::EB1b-GFP* [1] , *p35S::MAP4-GFP* [2] , *pSYP22::SYP22-YFP* [3] , *DR5::LUC* [4] , *PM-cyto* [5] marker lines were described previously. The *tir1-1/afb2-1/afb3-1* mutant [6] , *pTIR1::ccvTIR1* in *tir1-1/afb2-3* [7] , *pTIR1::TIR1* in *tir1-1/afb2-3* (we called it control for ccvTIR1) [7] and *aux1-100* [8,9] were donated by the authors. The *pTIR1::TIR1-VENUS* in *tir1-1* [10] , *pAFB1::AFB1-VENUS* in *afb1-3* [11] are shared by Stefan Kepinski. The *aha* mutants are the following: *aha2-5 (*SALK_022010), *aha1-7* (SALK_065288) [12] , *ost2-3D* shared by Atsushi Takemiya [13] . Two independent lines *AtTAS1c-AHA#2* and *#4* were generated by Jian Chen and Steffen Vanneste as follows: the syn-tasiRNA target sequence was inserted into *pENTR-AtTAS1c-B/c* [14] using hybridized primers TAS-AHA pair (Extended Data Table 4) and was recombined into *pH7m24GW* [15] together with *pDONR P4-P1R* carrying the *pPIN2* promoter [16] , to generate *pPIN2:AtTAS1c-AHA*. The *pAHA2::AHA2-GFP* seeds were donated by Anja T. Fuglsang [17] . The *tmk* mutants are the following: *tmk1- 1* (SALK_016360) [18] , *tmk4-1* (GABI_348E01) [19] ordered from NASC; Tongda Xu kindly contributed *tmk1- 2* (SAIL_812_G09), *tmk1-3* (SALK_008771) [20] , the complemented *pTMK1::gTMK1-FLAG* in *tmk1-1* [20] and *tmk1-1/tmk4-1* double mutant seeds. The transgenic plant lines carrying *DEX::TMK1-HA* and *DEX-TMK1-HA K616R* were generated by Hong Ren and William M. Gray. The DEX::TMK1 (or TMK1-K616R/E)-HA constructs were done by cloning the cDNA of TMK1 (or TMK1-K616R/E) without stop codon (Extended Data Table 4) into *pENTR/D-TOPO*, and subsequently recombining into the *pBAV154* [21] binary vector used Gateway system. The *pUBQ10::gTMK1-3HA* and *35S::gTMK1-eGFP* lines were generated by amplifying *TMK1* full length gDNA without stop codon from Col-0 genomic DNA using the primers indicated in Extended Data Table 4. *TMK1* gDNA was inserted into *pDONR221,* subsequently recombined into *pB7m34GW* together with *pDONR P4-P1R* carrying the *pUBQ10* promoter or *TMK1*

promoter and *pDONR P2R-P3 3xHA* or *pDONR P2R-P3 eGFP,* respectively. The constructs were transformed into the *Agrobacterium tumefaciens* strain pGV3101 by electroporation and further into Col-0 plants by floral dip.

Seeds were surface-sterilized by chlorine gas, sown on half-strength Murashige and Skoog (½ MS) medium supplemented with 1% (w/v) sucrose and 0.8% (w/v) phyto agar (pH 5.9), stratified in the dark at 4°C for 2 days and then grown vertically at 21°C with a long-day photoperiod (16h light/8h dark). Light sources used were Philips GreenPower LED production modules [in deep red (660 nm)/far red (720 nm)/blue (455 nm) combination, Philips], with a photon density of 140.4 μmol/m^2/s ± 3%.

Microfluidics

The microfluidic vRootchip was used to analyze root tip growth and apoplastic pH in real-time. The manufacturing of the chip, sample preparation procedure and data analysis of root tip growth were performed as described previously [22] . Our new design contains an additional valve in the control layer that closes the ends of the root channels (Extended Data Fig. 1m). In case of air bubbles in the root channels, the additional valve allows pressurizing the channel and air will be absorbed into the Polydimethylsiloxane (PDMS) chip material within 2-10 minutes. Afterwards, experiments started after adaptation of at least two hours. Besides, we introduced a graphical user interface (Extended Data Script 1) using the Processing software (https://processing.org/) with the ControlIP5 package (http://www.sojamo.de/libraries/controlP5/) that sends serial commands to the Arduino. A sketch (Extended Data Script 2) runs on the Arduino to operate the electronics and receive commands. For one vRootchip, maximum 8 samples were used. When comparing two genotypes, 3-4 seedlings were used for each genotype and mounted in alternating channels to minimize the time difference between imaging the two genotypes. For each root, we imaged one ROI containing early elongating epidermal cells and the other ROI covering the root tip. As these two ROIs were captured sequentially, we imaged the apoplastic pH and the growth of the same root close to simultaneously.

Scanner growth assay

To complement the real-time imaging in the vRootchip, growth analysis was performed on a vertical scanner with bigger sample sizes allowing more conditions to be evaluated. This growth measurement we called steady-state. 4-day-old seedlings were transferred to 60 × 15 mm petri dishes filled with 5 ml of ½ MS medium with treatments as indicated. The petri dishes were placed on a vertically mounted flatbed scanner (Epson perfection V370) and seedlings were imaged through the layer of medium. Either wet black filter paper or ½ MS medium containing activated charcoal was placed in the lid of the petri dishes to improve background contrast. The samples were automatically imaged every 10 or 30 minutes using the AutoIt script described previously [23] and scans were taken at 1200 dpi. The resulting image series were analyzed using StackReg stabilization and the Manual Tracking plugin in ImageJ.

Europe PMC Funders Author Manuscripts

Imaging and measuring apoplastic pH with HPTS dye

pH measurements were done both in steady-state condition and real-time vRootchip imaging. For steady-state pH analysis, 4-day-old seedlings were transferred to ½ MS medium containing 1 mM HPTS (Thermo Scientific 6358-69-6, dissolved in ddH_2O) and indicated treatments for 30 or 50 minutes as indicated. Subsequently, seedlings on a slice of the treatment medium were mounted into a Lab-Tek Chambered Coverglass for steady state imaging. Real-time imaging of the apoplastic pH was done in vRootchip containing medium (¼ MS + 0.1% sucrose) supplemented with 1mM HPTS with or without treatment. All imaging was performed on the in-house established vertical Zeiss LSM 800 confocal microscope [24] . Fluorescent signals for protonated HPTS (excitation 405 nm, emission 514 nm, visualized in red) and deprotonated HPTS (excitation, 488 nm, emission 514 nm, visualized in green) were detected with a 20x/0.8 air objective. Image analysis was performed on a cropped region of elongating epidermis cells using a batch processing modification of a previously described the ImageJ macro [25] . The relative pH value is calculated as the background-subtracted intensity of the deprotonated intensity divided by that of the protonated intensity to represent the relative pH. The resulting relative pH data were plotted over time and statistically evaluated in GraphPad Prism 6. Note that we did not transform the relative pH value to the absolute pH values, which would require the generation of a calibration curve for each experiment.

Imaging and measuring cytosolic pH with the PM-cyto reporter line

Real-time imaging of the cytosolic pH near the PM was done by using the *PM-cytp* reporter line in vRootchip containing medium (¼ MS + 0.1% sucrose), and was imaged on the in-house established vertical Zeiss LSM 800 confocal microscope [24] . Sequential illumination at 488 and 405 nm with emission 514 nm for both, corresponding to the two absorption peaks of pHluorin, were taken with a 20x/0.8 air objective. For each root in the vRootchip, two ROI with one containing the elongating epidermal cell for measuring the cytosolic pH and one containing the root tip for measuring the root growth rate were tracked over time. Image analysis was performed similar to the HPTS analysis described above.

Imaging microtubule orientation and vacuolar morphology

The *pEB1b::EB1b-GFP* maker line was used to track the dynamics of CMT orientation in vRootchip. Images were obtained every 6.25 s and the analysis of the CMT orientation was done in ImageJ by max Z-projection on every 10 frames and quantification by a for batch processing modified version of the Fibril Tool macro [26] . The *p35S::MAP4-GFP* marker line was used for capturing the CMT orientation after treatment for the indicated time period. The CMT orientation angle was processed using the Bioline script [27] . For both marker lines, the GFP (excitation 488 nm, emission 514 nm) signal was detected by Plan-Apochromat 20x/0.8 air objective in the vertical Zeiss LSM 800 confocal microscope [24] .

The *pSYP22::SYP22-YFP* marker line was used for imaging vacuolar morphology. We used a mounting system [28] , which allows the injection of new liquid medium during imaging. Images were taken before and 30 minutes after Mock or 100 nM IAA treatment in liquid medium and the YFP (excitation 488 nm, emission 527 nm) intensity was detected with C-Apochromat 40x/1.20 W Korr objective in an inverted Zeiss LSM 800 confocal microscope.

Non-invasive microelectrode (MIFE) ion flux measurements

Net H^+ flux was measured using non-invasive microelectrode ion flux estimation (MIFE) technique essentially as described elsewhere [29] . Roots of intact 6-day-old *Arabidopsis* WT seedlings were immobilised in a measuring chamber using Perspex holders. The composition of the solution was 0.5 mM KCl and 0.1 mM $CaCl_2$; pH 5.8, unbuffered. After 30-40 minutes of conditioning, the H^+ microelectrode was positioned 20 μm from the root surface in the elongation zone (~450 μm from the tip) (from which ion fluxes were measured). Steady-state H^+ fluxes were recorded for 5-10 minutes, and then 10 nM auxin treatment was applied following by another 30-40 minutes of recording. At least 9 individual plants from several batches were used. The sign convention is “influx positive”.

Evaluating the TIR1-transcriptional response using DR5::LUC

4-day-old DR5::LUC seedlings are placed on the surface of solidified ½ MS medium with 200 μl of 5 mM D-luciferin dissolved in 1x PBS drop on the root tips for 30 minutes as pre-treatment. Subsequently, the samples were transferred to the solidified ½ MS medium supplemented with mock, 10 nM IAA, 10 μM FC and IAA+FC, and immediately imaged in an in-house established dark box with a Photometric Evolve® EMCCD camera equipped with a 17 mm fixed lens/0.95 and an additional 125 mm lens [23] . The multiplier EMCCD gain was set to 70 and the exposure time to 35 sec, and images were acquired every 2 min. The resulting time-lapse video was analysed in ImageJ as described previously [23] .

Identification of TMK1-interacting proteins using IP/MS-MS

Immunoprecipitation (IP) experiments were performed in three biological replicates as described previously [30] using 1 g of roots of 7-day-old seedlings from the *p35S::TMK1-eGFP* transgenic line and 1 g of roots from WT. Interacting proteins were isolated by incubating total protein extracts with 100 μL anti-GFP coupled magnetic beads (Miltenyi Biotech). Three replicates of *p35S::TMK1-eGFP* were compared to three WT replicates. Tandem mass spectrometry (MS) on a Q-Exactive device (Thermo Fisher) and statistical analysis using MaxQuant and Perseus software was performed as described previously [31] .

Identification of TIR1- and AFB1-interacting proteins using IP/MS-MS

For immunoprecipitation, ground plant material of *pTIR1::TIR1-VENUS* in *tir1-1* and *pAFB1::AFB1-VENUS* in *afb1-3* transgenic lines was lysed in mild lysis buffer (50 mM Tris pH 7.5, 150 mM NaCl, 2 mM $MgCl_2$, 0.2 mM EDTA, 1xCPI, 0.5 mM DTT, 0.2% NP40 and 1 mg/ml DNAse) and mildly sonicated using a Bioruptor (Diagenode). After lysate clearance, supernatant was submitted to enrichment using GFP-Trap agarose beads (Chromotek) for 45 minutes at 4°C while gently rotating. Beads were subsequently washed twice in lysis buffer, twice in detergent-free lysis buffer and trice in 50 mM Ammoniumbicarbonate (ABC) (Sigma) with intermediate centrifuging for 2 minutes at 2000g at 4°C. After a final wash, bead-precipitated proteins were alkylated using 50 mM Acrylamide (Sigma). Precipitated proteins were submitted to on-bead trypsin digestion using 0.35 μg trypsin (Roche) per reaction. After overnight incubation at 25°C peptides were desalted and concentrated using C18 Stagetips.

After Stagetip processing, peptides were applied to online nanoLC-MS/MS using a 60 minutes acetonitrile gradient from 8-50%. Spectra were recorded on a LTQ-XL mass spectrometer (Thermo Scientific) according to [31] . Statistical analysis using MaxQuant and Perseus software was performed as described previously [31] .

Phospho-proteomics of auxin-treated roots

Roots from 5-day-old plants were treated and immediately harvested and flash frozen in liquid nitrogen. They then were ground to fine powder in liquid nitrogen. Powder was suspended in SDS lysis buffer (100 mM Tris pH8.0, 4%SDS and 10 mM DTT) and sonicated using a cooled Biorupter (Diagenode) for 10 minutes using high power with 30 seconds on 30 seconds off cycle. Lysate was cleared by centrifugation at maxiumum speed for 30 minutes. Protein concentrations were determined using the Bradford reagent (Bio-Rad).

For FASP 30 kDa cut-off amicon filter units (Merck Millipore) were used. Filters were first tested by appling 50 µl urea buffer UT buffer (8 M Urea and 100 mM Tris pH8.5) and centrifuging for 10 minutes at 11000 rpm at 20°C. The desired amount of protein sample was next mixed with UT buffer until a volume of 200 µl, applied to filter and centrifuged for 15 minutes. All centriguge steps were at 11000 rpm at 20°C. Filter was washed with UT buffer for 15 minutes. Retained proteins were alkylated with 50 mM acrylamide (Sigma) in UT buffer for 30 minutes at 20°C while gently shaking followed by a triple wash step with UT buffer for 15 minutes and three washes with 50 mM ABC buffer. After last wash proteins were cleaved by adding trypsin (Roche) in a 1:100 trypsin:protein ratio. Digestion was completed overnight. The following day filter was changed to a new tube and peptides were eluted by centrifuging for 15 minutes. Further elution was completed by adding two times 50 mM ABC buffer and centrifuging for 10 minutes on 11000 rpm at 20°C.

For peptide desalting and concentrating 200 µl tips were fitted with 2 plugs of C18 octadecyl 47 mm Disks 2215 (Empore™) material and 1 mg:10 µ*g* of LiChroprep® RP-18 : peptides (Merck). Tips were sequentially equilibrated with 100% methanol, 80% ACN in 0.1% formic acid and twice with 0.1% formic acid for 4 minutes at 1500g. After equilibration peptides were loaded for 20 minutes at 400g. Bound peptides were washed with 0.1% formic acid and eluted with 80% ACN in 0.1% formic acid for 4 minutes at 1500g. Eluted peptides were subsequently concentrated using a vacuum concentrator for 30 minutes at 45°C and resuspended in 50 µl of 0.1% formic acid.

For phosphopeptide enrichment magnetic Ti^{4+}-IMAC (MagResyn) were used according to manufactures protocol. Enrichments were perfromed with 1 mg of peptides in biological quadruplicate.

After Stagetip processing, peptides were applied to online nanoLC-MS/MS using a 120 minutes acetonitrile gradient from 8-50% for phospho-proteomics. Spectra recording and statistical analysis were as previously described, with the addition of phosphorylation as a variable modification [31] . Filtering of datasets was done in Perseus in as described [32] .

Phospho-proteomics in WT and *tmk1-1* roots

4 biological samples of Col-0 WT and *tmk1-1* roots were prepared and treated as indicated above. They were submitted to the phospho-proteomic pipeline [31,32] and differentially phosphorylated peptides belonging to H^+-ATPases were specifically filtered out of the big dataset (Extended Data Table 1).

Protein extraction and Western blot analysis for co-IP and determination of AHA2 phosphorylation state

To isolate PM H^+-ATPases and potential interactors, 5-7 day-old plant roots were harvested at the indicated time points after 10 or 100 nM IAA auxin treatment. 24 hour prior to the evaluation of auxin effects, these seedlings were sprayed with ½ AM solution containing 30 μM kynurenine. The root samples were flash frozen in liquid nitrogen and ground (Retsch mill, 2x 1 minute at 20 Hz). The root powder was then resuspended in a 1:1 (w/v) ratio in protein extraction buffer (25 mM Tris-HCl, pH 7.5, 150 mM NaCl, 1% Triton X-100, 1x Roche cOmplete™ Protease Inhibitor Cocktail, 1x Roche PhosSTOP™, 1 mM EDTA, 1 mM DTT and 0.5 mM PMSF). The samples were incubated on ice for 30 minutes, followed by a centrifuging step at 10,000*g* to discard the plant debris. The cleared supernatant containing the proteins of interest was collected and the total protein content was determined using Quick Start Bradford reagent (Bio-Rad). This could further be used for co-immunoprecipitation analysis or for SDS-PAGE analysis. In order not to lose relevant proteins, protein samples were not boiled in the presence of reducing Laemmli buffer and no harsher PM extraction or membrane enrichment was attempted.

For co-immunoprecipitation, root extracts (obtained by extraction in the Lysis buffer supplied in the Miltenyi μMACs kit, supplemented with 1x Roche cOmplete™ Protease Inhibitor Cocktail, 1 mM DTT and 0.5 mM PMSF), were incubated with magnetic beads from the Miltenyi anti-GFP, anti-HA or anti-FLAG μMACs kits (depending on the tags of the proteins of interest) and kept rotating for 4 hour at 4°C. Elution was performed with room-temperature denaturing elution buffer and the proteins were analyzed by SDS-PAGE and Western blot.

Following separation of proteins by SDS-PAGE in a 10% acrylamide gel (Protean® TGX™, Bio-Rad), proteins were transferred to PVDF membranes by electroblotting (Trans-blot® Turbo™, Bio-Rad). The membranes were then incubated in blocking buffer (0.05% Tween-20, 5% milk powder or 3% BSA, 20 mM Tris-HCl, pH 7.5 and 150 mM NaCl) for at least 60 minutes and incubated with antibody solution against the protein of interest.

Antibodies

The anti-AHA2 and anti-Thr^{947} AHA2 antibody were shared by Toshinori Kinoshita and used as described previously [33] at final dilution of 1:5000 in TBST buffer + 3% BSA, followed by anti-rabbit IgG secondary antibody conjugated to horseradish peroxidase (HRP) (GE Healthcare, NA934) at a dilution of 1:10000 and chemiluminescence reaction (SuperSignal West Femto, Thermo Scientific). To allow multiple antibody detections using the same PVDF membrane, mild stripping was performed using 15 g/L glycine, 1 g/L SDS, 10 mL/L Tween-20 buffer at pH 2.2 for 2-5 minutes.

ATP hydrolysis in root samples

To deplete endogenous auxin levels in the seedlings, 14-day-old plants were pre-treated with 30 μM kynurenine for 24 hour in the dark. Then, the pretreated seedlings were incubated in the presence and the absence of 100 nM indole-3-acetic acid for 60 minutes under dark condition. The roots excised from the seedlings were homogenized in the homogenization buffer (50 mM MOPS-KOH [pH 7.0], 100 mM KNO_3, 2 mM sodium molybdate, 0.1 mM NaF, 2 mM EGTA, 1 mM PMSF and 20 μM leupeptin) and the homogenates were centrifuged at 10,000 *g* for 10 minutes; the obtained supernatant was further ultra-centrifuged at 45,000 rpm for 60 minutes. The resultant precipitate (microsomal fraction) was resuspended in the homogenization buffer. ATP hydrolytic activity in the microsomal fraction was measured by the release of inorganic phosphate from ATP in a vanadate-sensitive manner following the method published [34] with the following modifications. The microsomal fraction (22.5 μL, 0.2 mg/mL) was mixed with the equal volume of the reaction buffer (60 mM MES-Tris [pH 6.5], 6 mM $MgSO_4$, 200 mM KNO_3, 1 mM ammonium molybdate, 10 μg/mL oligomycin, 2 mM NaN_3, 0.1% Triton X-100, 1 mM PMSF and 20 μM leupeptin) with or without 1 μL of 10 mM sodium orthovanadate. The reaction was started by adding 5 μL of 2 mM ATP and terminated by adding 50 μL of the stop solution (2.6% [w/v] SDS, 0.5% [w/v] sodium molybdate and 0.6 N H_2SO_4) after incubating at 30°C for 30 minutes.

Bimolecular Fluorescence Complementation (BiFC)

Following the method described [35] , the full-length coding sequences of AHA2 and TMK1 without stop codons were amplified by PCR (primers in Extended Data Table 4), cloned into *pENTR/D-TOPO* or *pDONR207* and recombined in *pSPYNE* and *pSPYCE* [36] to generate BiFC expression constructs. The resulting binary vectors were introduced in *Agrobacterium* GV3101 by electroporation and these were cultured until OD_{600} 0.8. Syringe infiltration was performed in *Nicotiana benthamiana* leaves as described in [37] . For the constructs of interest, final OD_{600} of 0.2 was used and p19 was co-infiltrated at OD_{600} 0.1 to avoid gene silencing. Infiltration buffer of pH5.8 contained: 10 mM $MgSO_4$, 10 mM MES-KOH and 0.15 mM acetosyringone. TMK1 overexpression, even transiently, has a strong effect on the viability of the leaves, so samples were taken daily after infiltration to determine the optimal balance between expression level and viable leaf cells. To visualize protein interactions, sections of the leaves were imaged using a Zeiss LSM 700 confocal microscope.

Quantitative RT-PCR

RNA was extracted from 5-day-old light-grown root tips with the RNAeasy Plant Mini Kit (Qiagen), with three biological replicates for each genotype. Two μg of RNA was used for cDNA synthesis (Qiagen). Samples were pipetted in three technical replicates using an automated JANUS Workstation (PerkinElmer) and measured by the Real-time PCR Roche LightCycler 480 using Luna® Universal qPCR mastermix (NEB, M3003S). Primers utilized for assessing gene expression are listed in Extended Table 4. Expression levels were normalized to Elongation factor 1-alpha (At5G60390) [37] .

Europe PMC Funders Author Manuscripts

Statistical analysis

All graphs were generated using GraphPad Prism 6 or 8. For statistical analysis of vRootchip data, Two-way ANOVA was performed for the entire time of x-axis except for indicated ones. Welch ANOVA analysis was applied for the scanner growth assays with multiple time points, and one-way ANOVA assays were used for steady state (one time point) pH and scanner growth datasets. Stars indicate significant differences on all graphs with ns for $p>0.05$, * for $p\leq0.05$, ** for $p\leq0.01$, *** for $p\leq0.001$ and **** for $p\leq0.0001$.

Europe PMC Funders Author Manuscripts

Extended Data

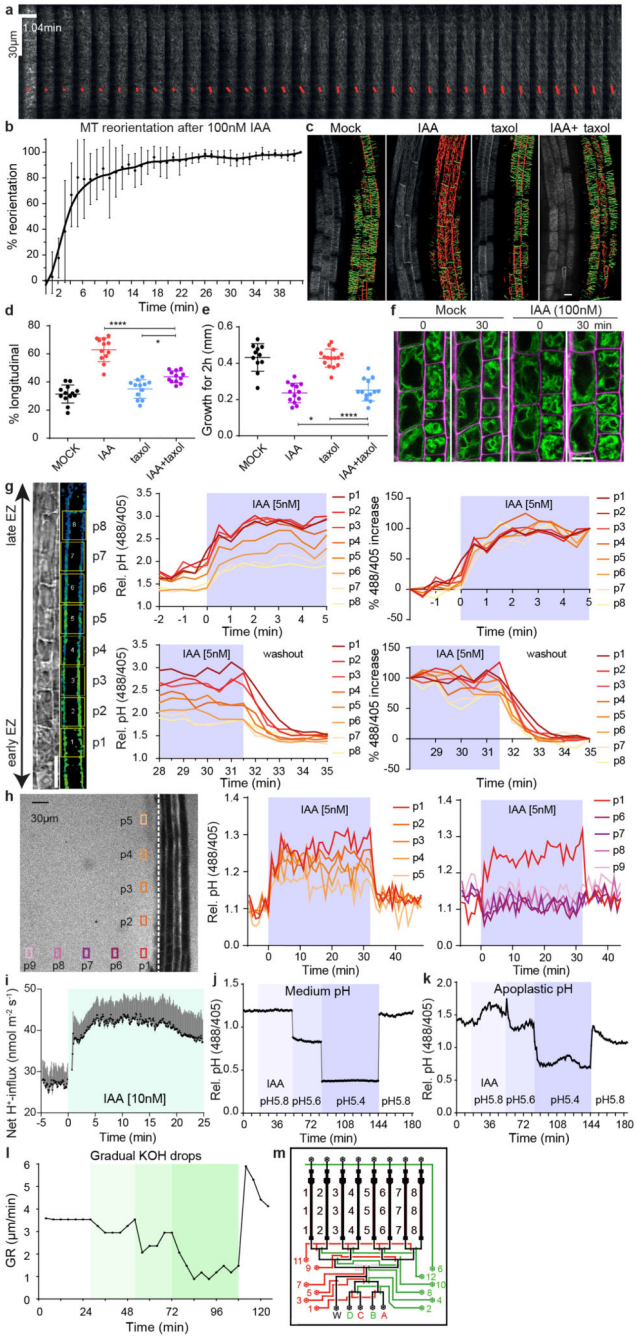

Extended Data Figure 1. Investigation of cellular mechanisms potentially involved in auxin-induced rapid root growth inhibition.

a-b, Dynamic cortical microtubule (CMT) reorientation in root cells from transversal to longitudinal in response to 100 nM IAA treatment. CMT was imaged in late elongating epidermal cells in the *pEB1b::EB1-GFP* marker line in vRootchip. Scans were made at 6.25 second intervals and a max Z-projection of 10 subsequent time frames was analysed using the FibrilTool macro. The average orientation of the microtubules is represented by the slope

of the red line and the length of the line represents its anisotropy (**a**). Quantification of CMT reorientation after 100 nM IAA treatment in (**a**). The percentage of CMT reorientation at every time point is calculated as the difference in the angle of that time point and the initial time point divided by the difference in the angles of the initial time point and end time point at 42 minutes. Mean of 5 elongating cells, ± SD (**b**).

c-e, Analysis of CMT reorientation in elongating epidermal root cells (**c, d**) and root growth (**e**) of *35S::MAP4-GFP* in response to 10 nM IAA, 10 μM taxol and IAA+taxol co-treatment. Orientation of CMT was analysed with the Bioline script. Green-colored CMTs mark transversal oriented CMT (angle between -45° and +45°), while red-colored CMTs indicate longitudinal orientation (angle between +45° and 135°). Scale bar = 15 μm (**c**). Quantification of (**c**) as the percentage of longitudinal CMT to total CMT detected. $n >$ 11, One-way ANOVA (**d**). Growth on respective treatments for 2 hours were measured. $n >$ 10, One-way ANOVA (**e**). *p≤0.05, ****p≤0.0001.

f, Vacuolar morphology tracked in the *pSYP22::SYP22-YFP* marker line (green signal) in the same elongating cells before and after 30 minutes of 100 nM IAA. Scale bar = 15 μm. Magenta signal indicates propidium-iodide stained cell walls.

g, Dynamics of apoplastic pH measured in different cells across the whole EZ (p1-p8) in vRootchip. The TL and blue-yellow scale image are from the same sample shown in Fig. 1a. Scale bar= 30 μm. The upper charts depict the dynamics of apoplastic pH in the indicated cells in response to 5 nM IAA, and the lower charts represent the pH in response to washout. The left two charts show the apoplastic pH measured by the HPTS dye. The right two charts show the speed at which each cell reaches its maximum pH change calculated as the difference between the pH at a given time point and the pre-stimulus pH, divided by the end pH change in that cell.

h, Dynamics of root surface pH and medium pH in vRootchip. Left graph shows the elongation zone of the root. The ROIs p1-p5 were chosen along the root, 30 μm away from the root surface indicated by the vertical white dotted line, while ROIs p6-p9 were distanced away from the root. The pH at the surface of the root (vertical positions p1-p5) increased after IAA and recovered after washout within 30 seconds. In contrast, the pH away from the root surface did not change significantly (horizontal positions p6-p9).

i, PM H^+-net influx measured by a non-invasive microelectrode before and after 10 nM IAA treatment in the elongating zone of WT roots. Means of 9 roots ± SD.

j-k, The medium pH (**j**) and apoplastic pH (**k**) changed rapidly after the exchange of the medium of different pH in vRootchip. Following media were used sequentially: basal medium at pH 5.8, auxin-containing medium at pH 5.8, gradually more acidic medium of pH 5.6, followed by pH 5.4 and lastly again basal medium at pH 5.8.

l, Quantification of root growth rate in response to the gradual addition of KOH in the medium in the vRootchip. The greener the shade, the more KOH was added followed by washout with the initial basal pH 5.8 medium.

m, Scheme of the modified vRootchip adding valve 6 and with valve routes adjusted.

Europe PMC Funders Author Manuscripts

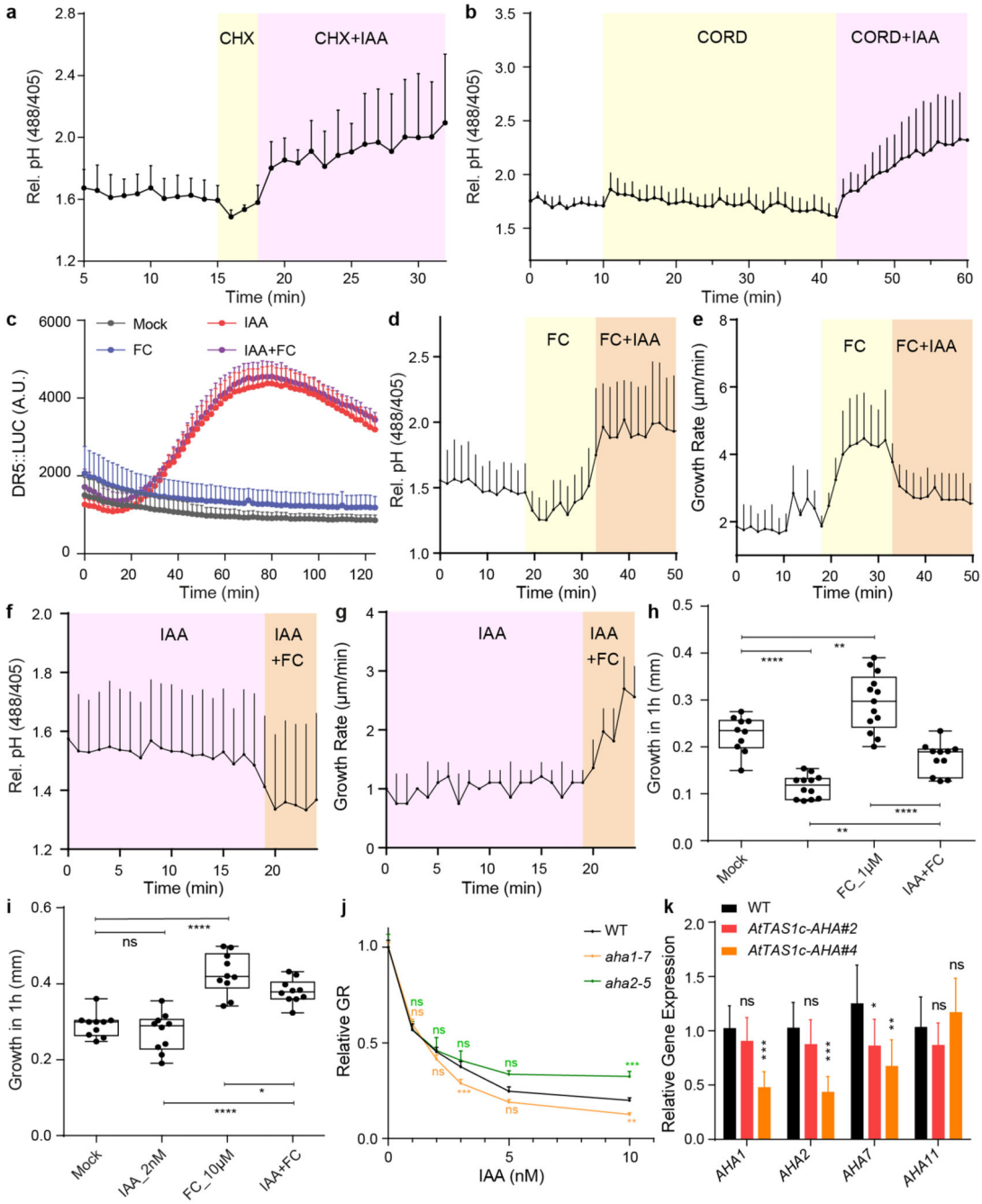

Extended Data Figure 2. H$^+$-ATPase activation counteracts auxin-mediated apoplast alkalinisation and growth inhibition

a, Measurement of luminescence intensity on the root tip of *DR5::LUC* line after 10 μM FC, 10 nM IAA and IAA+FC co-treatment. $n > 3$. IAA and IAA+FC are significantly different from the mock ($p \leq 0.0001$). No significant difference between IAA and IAA+FC ($p > 0.05$). Two-way ANOVA.

b-g, FC and IAA counteract each other. Addition of IAA still increased apoplastic pH (**b**) and inhibited root growth (**c**) in presence of FC in vRootchip. $n = 4$ (**b, c**). Addition of FC

still decreased the apoplastic pH (**d**) and promoted root growth (**e**) in presence of IAA in vRootchip. $n = 4$, the shaded area represents the duration time of the indicated treatments (**d-e**). Root growth after FC, IAA and co-treatment for 1 hour in steady state by scanner. 1 μM FC and 10 nM IAA were used in (**f**) while 10 μM FC and 2 nM IAA were used in (**g**). $n > 9$ for both graphs, ns p>0.05, *p≤0.05, **p≤0.01, ****p≤0.0001, One-way ANOVA (**f-g**).
h, Dose-response of auxin-induced root growth inhibition of *aha* single mutants. $n > 22$. Relative GR is ratio between auxin-affected growth in the mutant to mock growth for the same genotype. ns p>0.05, **p≤0.01, ***p≤0.001, Welch ANOVA.
i, Quantitative Real-time PCR on the *AHA1,2,7,11* expression in root tips of *AtTAS1c-AHA#2* and *#4*. The expression level was normalized to *EF1α* as housekeeping gene. Means of 3 biological replicates + SD.

Europe PMC Funders Author Manuscripts

Europe PMC Funders Author Manuscripts

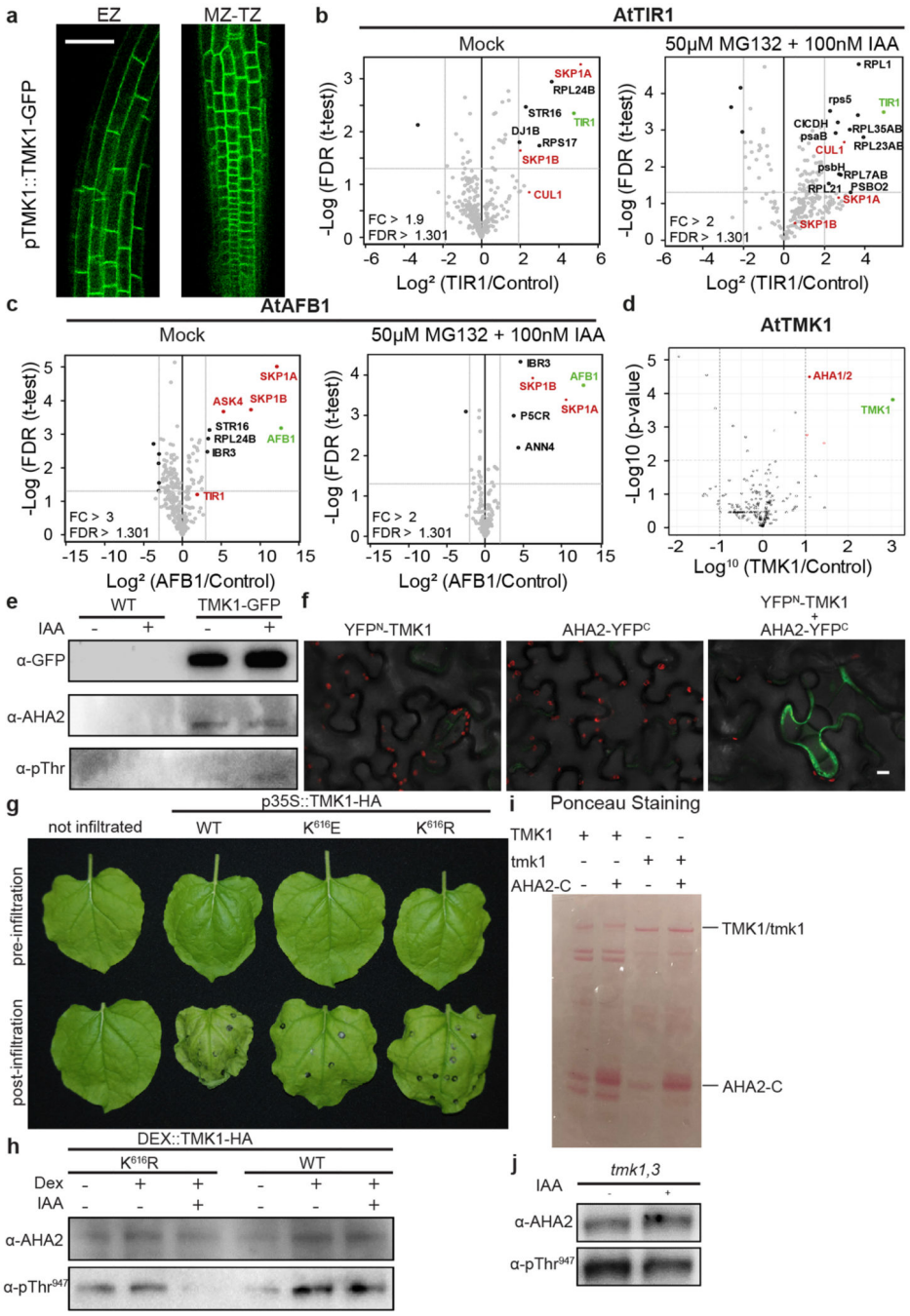

Extended Data Figure 3. TMK1 directly mediates auxin-induced H$^+$-ATPase activation.

a, IP-MS/MS on *pTIR1::TIR1-VENUS* in *tir1-1* and *pAFB1::AFB1-VENUS* in *afb1-3* lines under normal condition (upper graphs) compared to 1 hour 50 μM MG132 pre-incubation and 100nM IAA treatment for 2 minutes (lower graphs). Volcano plots show fold changes (in log^2 scale, x-axis) and significance (p-value, y-axis). Proteins passing the threshold of FDR 0.05 and specific fold change are marked. Green depicts the respective bait protein and red depicts known members of the SCF E3 ubiquitin ligase complex. Pulldowns were performed in triplicate, LFQ analysis.

b, IP-MS/MS on *35S::TMK1-GFP* line. Volcano plot shows fold change (in log^{10} scale, x-axis) and significance (p-value, y-axis). Red dots are in the range of ratio > 10 and -LOG p-value > 2. P-values are calculated based on the three replicates of *35S::TMK1-GFP* vs WT using a Two-sided t-test.

c, co-IP of *pTMK1::TMK1-GFP* roots, followed by Western blot detection of AHA2 and Thr^{947}-phosphorylated AHA2. The interaction was not regulated by 30 minutes of 100 nM IAA treatment, but the phosphorylation state of the interacting AHA2 was increased.

d, Bimolecular Fluorescent Complementation (BiFC) in *Nicotiana benthamiana* leaves transiently transformed with YFP^N-*TMK1*, *AHA2-*YFP^C or both. Scale bar = 10μm

e, Representation of wilting leaves of *Nicotiana benthamiana* that transiently express the WT TMK1 and ATP-site mutated forms: *p35S::TMK1-HA* $K^{616}E$ or $K^{616}R$.

f, Western blot analysis of the AHA2 levels and the Thr^{947} phosphorylation in roots of *DEX::TMK1*^{K616R}*-HA* and *DEX::TMK1-HA* lines treated +/- DEX (30 μM for 24 hours) and +/- IAA (100 nM for 1 hour).

g-h, Western blot detection of the AHA2 levels and the Thr^{947} phosphorylation in *tmk1,3* roots treated with 100 nM IAA for 1 hour (**g**). Quantification of the auxin effect on AHA2 phosphorylation in (**g**) by normalising the intensity ratio of $pThr^{947}$ to AHA2 detected in auxin-treated roots to the same ratio in mock-treated samples of the same genotype (**h**).

Europe PMC Funders Author Manuscripts

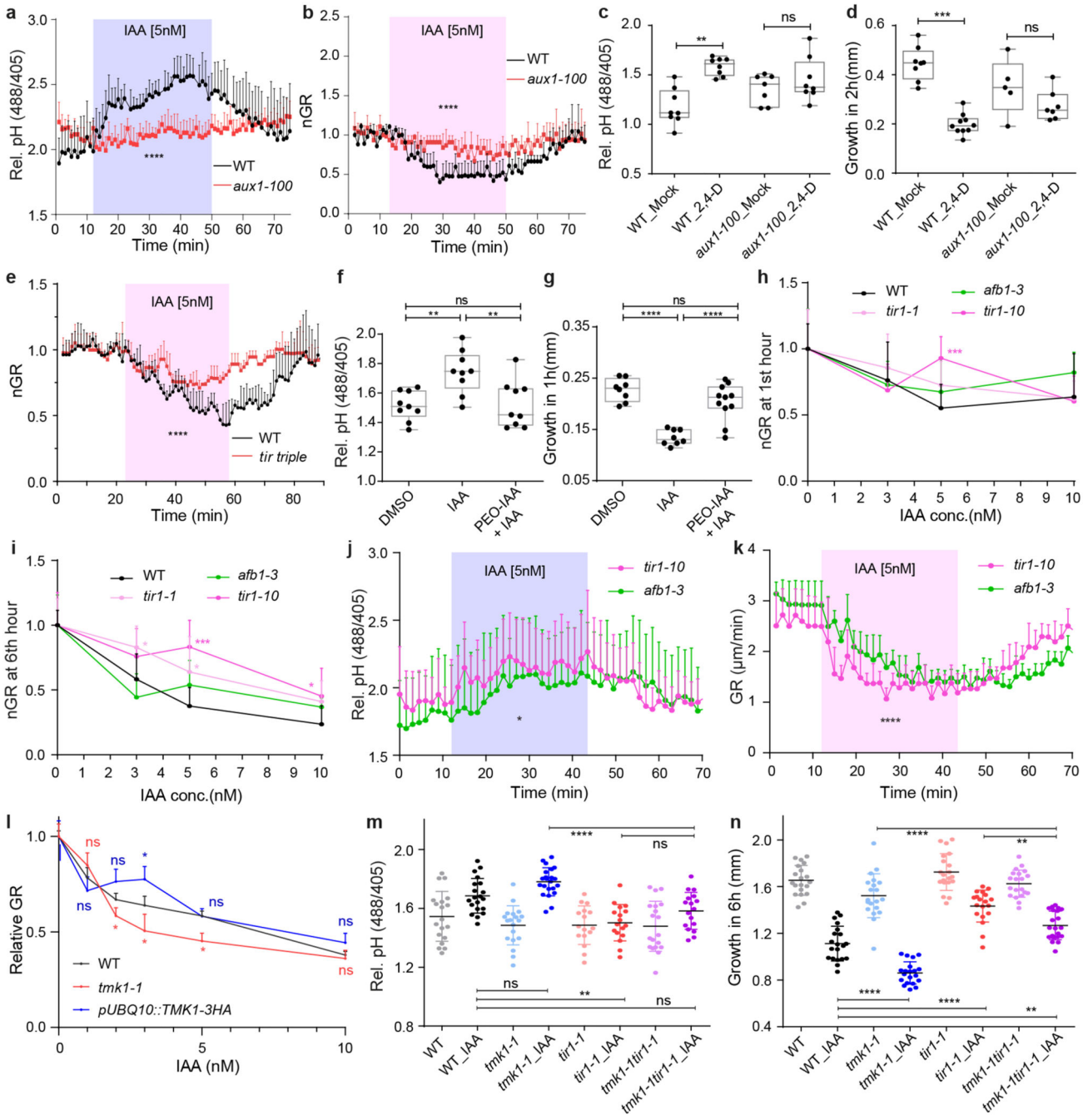

Extended Data Figure 4. TIR1/AFB and TMK1 signalling converge antagonistically on apoplastic pH and growth regulation.

a-b, Apoplastic alkalinisation (**a**) and root growth inhibition (**b**) in response to IAA measured in *aux1-100* mutant compared to WT roots in vRootchip. Apoplastic pH is measured by the HPTS dye. $n = 3$; $p \leq 0.0001$, Two-way ANOVA for both graphs.

c-d, Apoplastic alkalinisation (**c**) and root growth inhibition (**d**) in response to the synthetic auxin analogue 2,4-D in *aux1-100* mutant compared to WT roots. The steady state pH with the HPTS dye was measured 30 minutes after mock or 100 nM 2,4-D treatment. n > 6,

One-way ANOVA (**c**). The growth obtained in 2 hours was captured by scanner. $n > 4$, One-way ANOVA (**d**). ns p>0.05, **p≤0.01, ***p≤0.001.

e, Root growth of *tir triple* mutant (in red) compared to WT (in black) in response to 5 nM IAA in the vRootchip. $n = 3$, 2. p≤0.0001, two-way ANOVA.

f-g, apoplastic pH (**f**) and root growth (**g**) after 10 μM PEO-IAA and 5 nM IAA. The steady state pH was measured 30 minutes after the treatments using the HPTS dye, while the root growth obtained in 1 hour was recorded by scanning the plates. $n > 7$, ns p>0.05, **p≤0.01, ****p≤0.0001, One-way ANOVA.

h, Dose-response of auxin-induced root growth inhibition of *pUBQ10::TMK1-3HA* compared to WT and *tmk1-1*. Relative GR is the ratio between auxin-affected growth in a mutant to the mock growth for the same genotype. $n > 7$. ns p>0.05, *p≤0.05, Welch ANOVA.

i-j, Raw data for Figure 4d and e, respectively. ns p>0.05, **p≤0.01, ****p≤0.0001, One-way ANOVA.

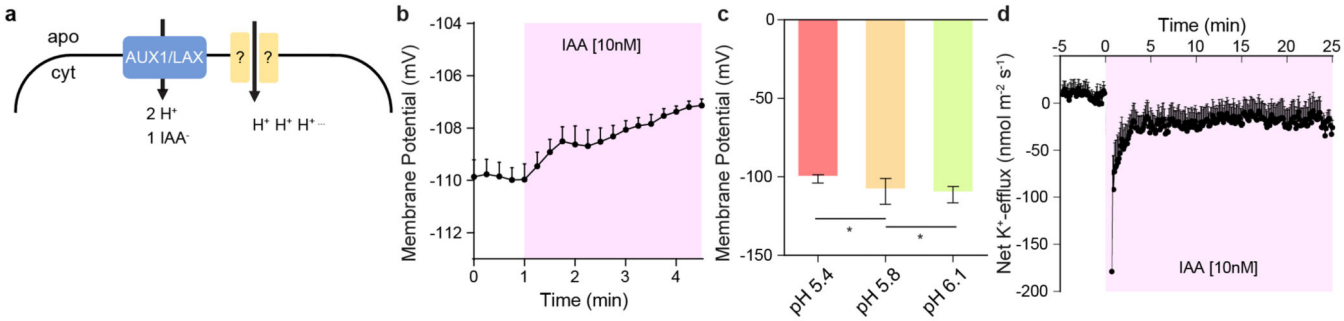

Extended Data Figure 5.

Europe PMC Funders Author Manuscripts

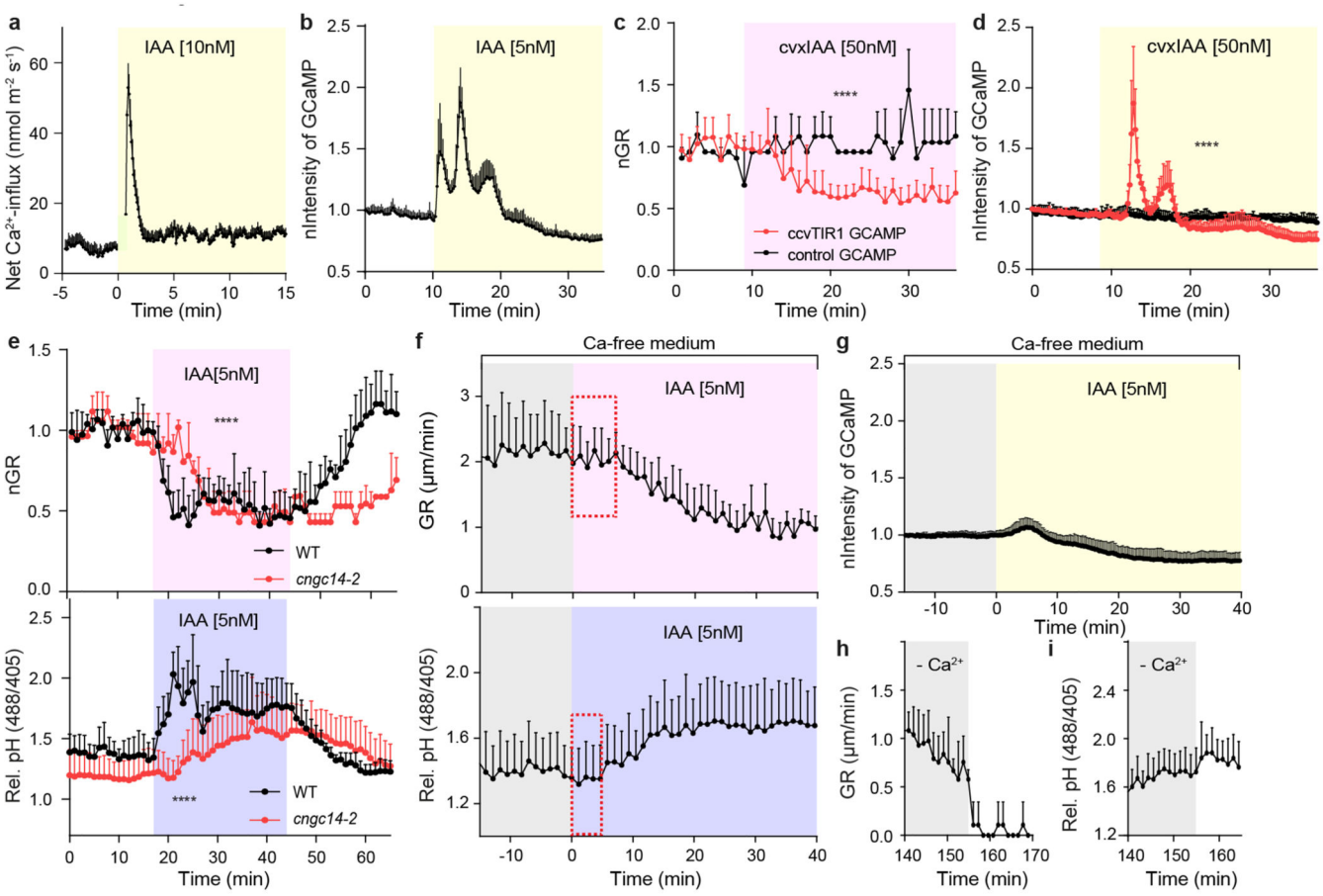

Extended Data Figure 6.

Extended Data Table 1

Phospho-proteomic data of rapid auxin effects in root and phospho-proteomic analysis of H^+-ATPases in *tmk1-1* mutants

Table contains differentially regulated phospho-peptides (FDR ≤0.05) in H^+-ATPases in IAA treated versus mock-treated roots. IAA treatment was at 100 nM for 2 minutes. QHF and LTQXL analysis are given in Tab 1 and 2, respectively. Tab 3 shows the differentially phosphorylated phospho-sites of AHAs in *tmk1-1* background compared to WT.

QHF analysis

FDR	LOG2(IAA/ mock)	Positions in prote	Gene names	Sequence window	Phospho (STY) Probabili
1.455	3.700	2	AHA1	_____MSGLEDIKNETVDLEKI	S(1)GLEDIKNETVDLEK
1.397	-0.564	881;817	AHA1	YGIGEREAQWAQAQRTLHGLQPKEDVNIFPET	(1)LHGLQPK
2.030	0.833	899;835	AHA1	GLQPKEDVNIFPEKGSYRELSEIAEQAKRRA	EDVNIFPEKGS(1)YR
1.397	-0.564	881;914	AHA2;HA2	YGKEEREAQWALAQRTLHGLQPKEAVNIFPE	T(1)LHGLQPK
2.403	0.753	899;932	AHA2;HA2	GLQPKEAVNIFPEKGSYRELSEIAEQAKRRA	EAVNIFPEKGS(1)YR

Europe PMC Funders Author Manuscripts

FDR	LOG2(IAA/mock)	Positions in prote	Gene names	Sequence window	Phospho (STY) Probabili
2.371	0.632	942;975	AHA2;HA2	GHVESVVKLKGLDIETPSHYTV_____	GLDIET(0.999)PS(0.001)I
1.403	-0.936	881;914;881;817	AHA2;HA2;AHA1	YGIGEREAQWAQAQRTLHGLQPKEDVNIFP E;YGKEEREAQWALAQRTLHGLQPKEAVNIF	T(1)LHGLQPK

Tab2
LTQXL analysis

FDR	LOG2(IAA/mock)	Positions within proteins	Gene names	Sequence w
4.482	1.823	881;914	AHA2;HA2	YGKEERE
2.044	1.314 947;980	AHA2;HA2	VVKLKGLDIETPSHYTV_____	
1.603	0.593	931;964;931;670;930;807;913;976;931;936;670;932	AHA2;HA2;AHA6;AHA8;HA9;AHA5;AHA9;AHA3	IARLRELH

Tab3
WT vs *tmk1-1*

Pos	FDR	LOG2(*tmk1-1*/WT)	hyper/hypo in *tmk1-1*	Known function	Gene names	Sequence window	Phospho (STY) Probabi
881	2.800	-0.693	hypo	activation	AHA1 or AHA2;HA	YGIGEREAQWAQAQRTLHGLQPKEDVNIFPE	T(1)LHGLQPK
882	3.120	-1.478	hypo	activation	AHA3	YGIEEREAQWAHAQRTLHGLQNTETANVVPE	T(1)LHGLQNTETANV
948	3.034	-0.621	hypo	activation	AHA1	AKLKGLDIDTAGHHYTV_____	GLDIDTAGHHYT(1)V
947	3.646	-1.025	hypo	activation	AHA2;HA2	VVKLKGLDIETPSHYTV_____	LKGLDIETPSHYT(1)V
948	2.653	-1.783	hypo	activation	AHA3	VVKLKGLDIETAGHYTV_____	GLDIETAGHYT(1)V
899	2.913	-0.576	hypo	inhibitory	AHA1	GLQPKEDVNIFPEKGSYRELSEIAEQAKRRA	EDVNIFPEKGS(1)YR
899	2.004	-0.461	hypo	inhibitory	AHA2;HA2	GLQPKEAVNIFPEKGSYRELSEIAEQAKRRA	EAVNIFPEKGS(1)YR
931	3.546	1.813	hyper	inhibitory	AHA1	IARLRELHTLKGHVESVAKLKGLDIDTAGHH	GHVES(1)VAK
942	3.922	-0.385	hypo	n/a	AHA2;HA2	GHVESVVKLKGLDIETPSHYTV_____	GLDIET(0.998)PS(0.002
955	6.383	-3.999	hypo	n/a	AHA11;AHA4	VRLKGLDIETIQQAYTV_____	GLDIETIQQAYT(1)V

Europe PMC Funders Author Manuscripts

Extended Data Table 2
IP-MS analysis of *pTIR1::TIR1-VENUS* and *pAFB1::AFB1-VENUS*

Overview of the putative TIR1 and AFB1 interactors after MaxQuant and Perseus statistical analysis. Samples were TIR1 and AFB1-Venus lines under mock, 50 μM MG132 pre-incubation for 1 hour and 100 nM IAA treatment for 2 minutes. Proteins passing the threshold of FDR 0.05 and specific fold change are included in the table. P-values are calculated based on the three replicates using a Two-sided t-test. Pulldowns were performed in triplicate. Yellow highlight indicates the respective bait protein.

TIR1 with Mock

LQG2(TIR1/Control)	X-LQG10FDI	Peptides	Student's T-test	Majority protein IDs	Protein names
5.118258158	3.27648164	17	10.15708944	Q39255	SKP1-like protein 1A
4.754890442	2.34634325	10	5.760780734	Q570C0	Protein TRANSPORT INHIBITOR RESPONSE 1
3.60787646	2.94711492	2	8.340412262	P38666;Q42347	60S ribosomal protein L24-2;60S ribosomal protein L24-1
2.98809878	1.73797235	2	3.851309445	P16180	30S ribosomal protein S17, chloroplastic
2.459372203	0.85221949	2	1.834243789	Q94AH6	Cullin-1
2.273972829	2.46638828	2	6.212296758	F4JZ17;Q39129	Thiosulfate sulfurtransferase 16, chloroplastic
2.201576869	0.96994873	2	2.070539977	Q42431	Oleosin 20.3 kDa
2.001925786	0.87062371	4	1.870823782	F4JVC0;F4JVC1;Q03251;F4JV	Glycine-rich RNA-binding protein 8
1.988611857	1.64404399	15	3.603054736	Q9FHW7	SKP1-like protein 1B
1.940104802	1.79712208	3	4.013188676	Q9MAH3	Protein DJ-1 homolog B
1.933815002	0.86164735	2	1.852967808	P59230;Q8VZB9;P59231	60S ribosomal protein L10a-2;60S ribosomal protein L10a-1;60S ribosomal protein L10a-3
1.823474248	1.06487476	2	2.2658229	Q8LA13;Q84W89;Q9M2F9	DEAD-box ATP-dependent RNA helicase 1 1;DEAD-box ATP-dependent RNA helicase 37;DEAD-box ATP-dependent RNA helicase 52
1.708749771	0.93651248	3	2.002836801	P16127;Q5XF33	Magnesium-chelatase subunit ChlI-1, chloroplastic;Magnesium-chelatase subunit ChlI-2, chloroplastic
1.60286204	1.15507001	2	2.456251697	Q9LU14	GDSL esterase/lipase APG

Europe PMC Funders Author Manuscripts

Tab2
TIR1 with MG132+IAA

LOG2(TIR1/ Contro	X-LQG10FDI	Peptides	Majority protein IDs	Protein names
4.927825928	3.49271141	8	Q570C0	Protein TRANSPORT INHIBITOR RESPONSE 1
3.933736801	2.80313389	2	A8MS83;Q9M3C3;Q8LD46	60S ribosomal protein L23a-2;60S ribosomal protein L23a-1
3.685892105	4.80039226	4	Q9LY66;F4J296	50S ribosomal protein L1, chloroplastic;Ribosomal protein
3.657317479	3.40802567	2	Q94F20;Q9LYE7	
3.300284704	1.30913348	9	Q9S841	Oxygen-evolving enhancer protein 1-2, chloroplastic
3.252434413	3.01858947	1	Q9FZH0;P51422;Q9LMK0;Q9C912	60S ribosomal protein L35a-2;60S ribosomal protein L35a-4;60S ribosomal protein L35a-1;60S ribosomal protein L35a-3
3.030831655	1.22114312	7	F4K5C7;Q93VH9;Q8VYK6;P49204;F4IMI	40S ribosomal protein S4;40S ribosomal protein S4-1;40S ribosomal protein S4-3;40S ribosomal protein S4-2
2.978437424	2.67620031	4	Q94AH6	Cullin-1
2.882202148	0.94348696	5	O65282	20 kDa chaperonin, chloroplastic
2.844031016	1.06575137	8	O50008;Q9SRV5	5-methyltetrahydropteroyltriglutamate--homocysteine methyltransferase 1;5-methyltetrahydropteroyltriglutamate--homocysteine methyltransferase 2
2.810997645	1.77625477	2	Q9LZH9;P49692	60S ribosomal protein L7a-2;60S ribosomal protein L7a-1
2.78762118	0.85362368	3	P56779	Cytochrome b559 subunit alpha
2.732335409	0.99431437	4	P56761	Photosystem II D2 protein
2.729720434	1.80469265	1	P56780	Photosystem II reaction center protein H
2.696318944	1.16176096	15	Q39255	SKP1-like protein 1A
2.654738108	3.21512215	3	Q9SRZ6	Cytosolic isocitrate dehydrogenase [NADP]
2.62142245	0.88366927	14	P56777	Photosystem II CP47 reaction center protein
2.577622732	1.27224002	4	P49200;Q9STY6	40S ribosomal protein S20-1;40S ribosomal protein S20-2
2.557145437	2.92182336	2	P56767	Photosystem I P700 chlorophyll a apoprotein A2
2.468788783	1.02031666	2	P59224;P59223	40S ribosomal protein S13-2;40S ribosomal protein S13-1

Tab3
AFB1 with Mock

LOG2(AFB1/ Contro	X-LOG10FDR	Peptides	Majority protein IDs	Protein names
12.71776517	3.186698841	39	Q9ZR12	GRR1-like protein 1
12.1318264	5.01302371	17	Q39255	SKP1-like protein 1A
8.830174764	3.734570639	15	Q9FHW7	SKP1-like protein 1B
5.277590434	3.678132585	4	Q9LNT9	SKP1-like protein 4
3.481123606	3.122493649	2	F4JZ17;Q39129	Thi osulfate sulfurtransferase 16, chloroplastic
3.299066544	2.864853421	2	P38666;Q42347	60S ribosomal protein L24-2;60S ribosomal protein L24-1
3.181758245	2.478213172	4	Q8RWZ3	Probable acyl-CoA dehydrogenase IBR3
2.674465815	0.602639535	9	Q96318;F4JLA9;A0A1	12S seed sto rage protein CRC;12S seed sto rage protein CRC alpha chain;12S seed storage protein CRC beta chain
2.493788401	1.366144629	4	A0A1I9LR27;F4JBC9;	Peroxiredoxin Q, chloroplastic
2.472199122	1.72041483	2	Q9LIK9;A0A1P8B8I9	ATP sulfurylase 1, chloroplastic;ATP-sulfurylase 3, chloroplastic;ATP;Osulfurylase 2
2.393953959	1.62946189	2	F4J3P1;P49690	60S ribosomal protein L23
2.321870804	0.796044035	4	F4JVC0;F4JVC1;Q032	Glycine-rich RNA-binding protein 8
2.203902562	2.8275101	3	P54150	Peptide methionine sulfoxide reductase A4, chloroplastic
2.177773158	0.688776393	2	Q9XEX2;F4ID64	Peroxiredoxin-2B
2.140075048	1.556645965	3	Q9MAH3	Protein DJ-1 homolog B
2.124917984	2.740719054	8	Q9FPF0	Protein DJ-1 homolog A
1.950544993	2.509962048	8	Q42403	Thioredoxin H3
1.90527916	1.200714146	10	Q570C0	Protein TRANSPORT INHIBITOR RESPONSE 1
1.868207932	2.585869519	4	F4JRT7;Q9SW21	Acyl carrier protei n;Acyl carrier protein 4, chloroplastic
1.83743159	2.210789882	4	Q9LMU2	

Tab4
AFB1 with MG132+IAA

LOG2(AFB1/ Contro	X-LOG10FDF	Unique peptide	Majority protein IDs	Protein names
12.90374565	3.74151941	40	Q9ZR12	GRR1-like protein 1
10.63748741	3.38102284	10	Q39255	SKP1-like protein 1A
6.259954453	3.92243778	7	Q9FHW7	SKP1-like protein 1B
4.639073054	4.3296288	10	Q8RWZ3	Probable acyl-CoA dehydrogenase IBR3
4.359214783	2.19487358	4	A0A1P8B1L4;Q9ZVJ6	Annexin D4
3.768214544	2.99147254	3	F4K884;P54904	Pyrroline-5-carboxylate reductase

LOG2(AFB1/ Contro	X-LOG10FDF	Unique peptide	Majority protein IDs	Protein names
1.720092138	0.82292309	2	Q9LFH5;P50883;Q9F	60S ribosomal protein L12-2;60S ribosomal protein L12-1;60S ribo
1.644043605	0.73016299	2	Q9T043;Q9SIM4	60S ribosomal protein L14-2;60S ribosomal protein L14-1
1.637237549	0.71121767	8	O50008;Q9SRV5	5-methyltetrahydropteroyltriglutamate--homocysteine methyltransfe
1.612161636	1.66766713	3	P22953;F4KCE5	Probable mediator of RNA polymerase II transcription subunit 37e
1.431067149	1.70145982	6	P59259;A8MRV1	Histone H4
1.361975988	0.88519951	4	P49200;Q9STY6	40S ribosomal protein S20-1;40S ribosomal protein S20-2
1.265961965	1.72620153	3	Q56WH1;B9DHQ0	Tubulin alpha-3 chain;Tubulin alpha-5 chain
1.181111018	0.8679059	4	Q06588	1 -aminocyclopropane-1 -carboxylate oxidase 4
1.174767812	1.24492756	3	O04314	PYK10-binding protein 1
0.979935964	0.54012105	2	P42795;P42794	60S ribosomal protein L11-1;60S ribosomal protein L11-2
0.946492513	0.61817655	2	P59224;P59223	40S ribosomal protein S13-2;40S ribosomal protein S13-1
0.933000565	1.33895745	2	O23049	50S ribosomal protein L6, chloroplastic
0.860973358	0.25342145	1	Q9LTX9	Heat shock 70 kDa protein 7, chloroplastic
0.841140111	0.42174345	3	Q9SCX3	Elongation factor 1-beta 2

Extended Data Table 3
IP-MS analysis of *p35S::TMK1-GFP*.

Overview of the putative TMK1 interactors after MaxQuant and Perseus statistical analysis. The list is sorted based on the ratio of *35S::TMK1-GFP* vs WT control. Proteins passing the threshold of FDR 0.05 and specific fold change are included in the table. P-values are calculated based on the three replicates using a two-sided t-test. Yellow highlight indicates bait, green indicates GFP and orange indicates selected proteins.

Average V	Average TM	Ratio	P-value	Fasta.headers
4.68	7.67	963.19	9.27E-05	Symbols: TMK1 | transmembrane kinase 1 | chr1:24631503-24634415 FORWARD LENG
5.59	6.98	24.32	2.77E-01	Symbols: | Protein prenylyltransferase superfamily protein | chr5:5679995-5685597 FORW
4.51	5.85	21.80	3.99E-03	Symbols: PGP10 | P-glycoprotein 10 | chr1:3538470-3543782 REVERSE LENGTH=1227;
4.64	5.81	14.75	3.25E-02	Symbols: PIP2F, PIP2;4 | plasma membrane intrinsic protein 2;4 | chr5:24375673-2437693
6.01	7.11	12.53	3.11E-05	Symbols: AHA1, PMA, OST2, HA1 | H(+)-ATPase 1 | chr2:8221858-8227268 FORWARD
5.06	6.10	10.99	1.34E-01	ALDOA_RABIT | Fructose-bisphosphate aldolase A (EC 4.1.2.13) (Muscle-type aldolase)

Average V	Average TM	Ratio	P-value	Fasta.headers
5.84	6.87	10.73	1.74E-03	Symbols: TMP-C, PIP1;4, PIP1E | plasma membrane intrinsic protein 1;4 | chr4:186569-18
5.38	6.21	6.75	4.73E-02	Symbols: PIP2B, PIP2;2 | plasma membrane intrinsic protein 2 | chr2:15613624-15614791
6.91	7.67	5.80	3.66E-04	Symbols: | Mannose-binding lectin superfamily protein | chr5:14090825-14092808 FORWA
5.19	5.95	5.69	1.11E-01	Symbols: MED19A | MED19A;BEST Arabidopsis thaliana protein match is: unknown protei
5.60	6.36	5.67	2.41E-01	Symbols: | Translation protein SH3-like family protein | chr1:3136407-3137430 REVERSE
5.86	6.59	5.46	2.91E-01	LYSC_CHICK | Lysozyme C (EC 3.2.1.17) (1,4-beta-N-acetylmuramidase C) (Allergen Gal
5.55	6.26	5.21	2.42E-01	Symbols: | Translation protein SH3-like family protein | chr3:18504311-18504751 FORWA
5.69	6.36	4.69	3.21E-01	Symbols: | Ribosomal protein S5 domain 2-like superfamily protein | chr5:6090128-609069
4.89	5.49	4.05	9.96E-02	Symbols: PIP2A, PIP2, PIP2;1 | plasma membrane intrinsic protein 2A | chr3:19803906-19
7.24	7.82	3.74	1.39E-01	GFP AEQV1 | Green fluorescent protein;eGFP from pK7WGF2;eGFP from pK7FWG2;GF

Extended Data Table 4
Primers used for cloning and qPCR analysis

Name	Direction	Sequence	Gene ID	Purpose
pTMK1	Fw	GGGGACAACTTTGTATAGAAAAGTTGCATCGTTTGGAACAGATCTTTCAGC	AT1G66150	for cloning TMK1 promoter
	Rv	GGGGACTGCTTTTTTGTACAAACTTGCAGCTTGAAGAAACAGAGGATTGAAG		
gTMK1	Fw	GGGGACAAGTTTGTACAAAAAAGCAGGCTCAATGAAGAAAAGAAGAACCTT	TAT1G66150	for cloning genomic TMK1
	Rv	GGGGACCACTTTGTACAAGAAAGCTGGGTCTCGTCCATCTACTGAAGTGAAT		
cTMK1	Fw	caccATGAAGAAAAGAAGAACCTTTC	AT1G66150	for cloning cDNA of TMK1
	Rv	TCGTCCATCTACTGAAGTGAATG		
cTMK1-K616R	Fw	CGAAGATTGCGGTTAGGAGAATGGAGAATGG	AT1G66150	for cloning cDNA of TMK1-K616
	Rv	CCATTCTCCATTCTCCTAACCGCAATCTTCG		
cTMK1-K616E	Fw	CGAAGATTGCGGTTGAGAGAATGGAGAATG	AT1G66150	for cloning cDNA of TMK1-K616
	Rv	CATTCTCCATTCTCTCAACCGCAATCTTCG		
TAS_AHA	Fw	CCTTTTTCTCCATGACCCTATGCATTTTACCAA	same gene ID as in qPCR	for cloning syn-tasiRNA target sequence
	Rv	GTTCTTGGTAAAATGCATAGGGTCATGGAGAAAAAGGAGAGTAAGAATGT GAAAAAGTTGCAGGAGAATGTGAAAAAGCTGCAGGAGA		

Name	Direction	Sequence	Gene ID	Purpose
				targeting AHA1/2/7/11
qEF1a	Fw	TGAGCACGCTCTTCTTGCTTTCA	AT5G60390	for qrtPCR
	Rv	GGTGGTGGCATCCATCTTGTTACA		
qAHA1	Fw	GCCAGCTTGTTTGACAACAGGAC	AT2G18960	for qrtPCR
	Rv	TTTGGCTGCAGACCGTGCAATG		
qAHA2	Fw	ACATTGACGGCAGTGGTAACTGG	AT4G30190	for qrtPCR
	Rv	TTTGGCAAGTTCGAGGATCTGC		
qAHA7	Fw	TGCTCTAAGTGGCAAATCATGGG	AT3G60330	for qrtPCR
	Rv	TTCTTTCCTGTGAGTGCAGTCCTC		
qAHA11	Fw	CATTGGCGGTATCCCAATTGCC	AT5G62670	for qrtPCR
	Rv	CCTCTTGGTTATTGCTCCCTGCTG		

Supplementary Material

Refer to Web version on PubMed Central for supplementary material.

Acknowledgements

We thank Nadine Paris for sharing the PM-Cyto seeds, Lukas Hörmayer for help with the auxin sensitivity assay analysis. This research was possible thanks to the Scientific Service Units (SSU) of IST-Austria through resources provided by the Bioimaging Facility (BIF). In particular, we are grateful to Judit Singer for improving the vertical microscope stage for the vRootchip imaging chamber, to Yann Cesbron for modifying the ratiometric fluorescence script for pH analysis and to Robert Hauschild for modifying the Fibril tool script for CMT analysis. The Austria IST machine shop we thank for constructing the vRootchip imaging chamber. This project has received funding from the European Research Council Advanced Grant (ETAP-742985), the Austrian Science Fund (FWF) I 3630-B25, and the National Institutes of Health (GM067203 to W.M.G.). W.S. and B.D.R. were funded by the Netherlands Organization for Scientific Research (NWO; VIDI-864.13.001), The Research Foundation - Flanders (FWO; Odysseus II G0D0515N) and a European Research Council Starting Grant (TORPEDO-714055). M.R and D.W. were funded by a VICI grant (865.14.001) from the Netherlands Organization for Scientific Research. S.S. acknowledges the financial support from the Australian Research Council and China National Distinguished Expert Project (WQ20174400441). K.T. (20K06685) and T.K. (20H05687 and 20H05910) were funded by MEXT/JSPS KAKENHI. L.L was funded by the European Union's Horizon 2020 research and innovation programme under the Marie Skłodowska-Curie Grant Agreement No. 665385 and the DOC Fellowship of the Austrian Academy of Sciences.

References

1. Spartz AK, et al. SAUR inhibition of PP2C-D phosphatases activates plasma membrane H^+-ATPases to promote cell expansion in Arabidopsis. Plant Cell. 2014; 26: 2129–2142. [PubMed: 24858935]
2. Rayle DL, Cleland R. Enhancement of wall loosening and elongation by acid solutions. Plant Phys. 1970; 46: 250–253.
3. Hager A, Menzel H, Krauss A. Versuche und hypothese zur primärwirkung des auxins beim streckungswachstum. Planta. 1971; 100: 47–75. [PubMed: 24488103]
4. Du M, Spalding EP, Gray WM. Rapid auxin-mediated cell expansion. Annu RevPlant Biol. 2020; 71: 379–402.
5. Fendrych M, Leung J, Friml J. TIR1/AFB-Aux/IAA auxin perception mediates rapid cell wall acidification and growth of Arabidopsis hypocotyls. Elife. 2016; 5 e19048 [PubMed: 27627746]
6. Chapman EJ, Estelle M. Mechanism of auxin-regulated gene expression in plants. Annu Rev Genet. 2009; 43: 265–285. [PubMed: 19686081]

7. Uchida N, et al. Chemical hijacking of auxin signaling with an engineered auxin–TIR1 pair. Nat Chem Biol. 2018; 14: 299. [PubMed: 29355850]
8. Pickett FB, Wilson AK, Estelle M. The aux1 mutation of Arabidopsis confers both auxin and ethylene resistance. Plant Phys. 1990; 94: 1462–1466.
9. Fendrych M, et al. Rapid and reversible root growth inhibition by TIR1 auxin signalling. Nat Plants. 2018; 4: 453. [PubMed: 29942048]
10. Cao M, et al. TMK1-mediated auxin signalling regulates differential growth of the apical hook. Nature. 2019; 568: 240–243. [PubMed: 30944466]
11. Chen X, et al. Inhibition of cell expansion by rapid ABP1-mediated auxin effect on microtubules. Nature. 2014; 516: 90. [PubMed: 25409144]
12. Adamowski M, Li L, Friml J. Reorientation of cortical microtubule arrays in the hypocotyl of Arabidopsis thaliana is induced by the cell growth process and independent of auxin signaling. Int J Mol Sci. 2019; 20: 3337.
13. Scheuring D, et al. Actin-dependent vacuolar occupancy of the cell determines auxin-induced growth repression. PNAS. 2016; 113: 452–457. [PubMed: 26715743]
14. Barbez E, Dünser K, Gaidora A, Lendl T, Busch W. Auxin steers root cell expansion via apoplastic pH regulation in Arabidopsis thaliana. PNAS. 2017; 114: E4884–E4893. [PubMed: 28559333]
15. Monshausen GB, Miller ND, Murphy AS, Gilroy S. Dynamics of auxin-dependent Ca^{2+} and pH signaling in root growth revealed by integrating high-resolution imaging with automated computer vision-based analysis. Plant J. 2011; 65: 309–318. [PubMed: 21223394]
16. Shih H-W, DePew CL, Miller ND, Monshausen GB. The cyclic nucleotide-gated channel CNGC14 regulates root gravitropism in Arabidopsis thaliana. Curr Biol. 2015; 25: 3119–3125. [PubMed: 26752079]
17. Von Wangenheim D, et al. Live tracking of moving samples in confocal microscopy for vertically grown roots. Elife. 2017; 6 e26792 [PubMed: 28628006]
18. Martinière A, et al. Uncovering pH at both sides of the root plasma membrane interface using noninvasive imaging. PNAS. 2018; 115: 6488–6493. [PubMed: 29866831]
19. Fuglsang AT, et al. Receptor kinase-mediated control of primary active proton pumping at the plasma membrane. Plant J. 2014; 80: 951–964. [PubMed: 25267325]
20. Haruta M, Gray WM, Sussman MR. Regulation of the plasma membrane proton pump (H^+-ATPase) by phosphorylation. Curr Opin Plant Biol. 2015; 28: 68–75. [PubMed: 26476298]
21. Kinoshita T, Shimazaki Ki. Blue light activates the plasma membrane H^+-ATPase by phosphorylation of the C-terminus in stomatal guard cells. EMBO J. 1999; 18: 5548–5558. [PubMed: 10523299]
22. Takahashi K, Hayashi K-i, Kinoshita T. Auxin activates the plasma membrane H^+-ATPase by phosphorylation during hypocotyl elongation in Arabidopsis. Plant Phys. 2012; 159: 632–641.
23. Fuglsang AT, et al. Binding of 14-3-3 protein to the plasma membrane H^+-ATPase AHA2 involves the three C-terminal residues Tyr^{946}-Thr-Val and requires phosphorylation of Thr^{947} . J Biol Chem. 1999; 274: 36774–36780. [PubMed: 10593986]
24. Svennelid F, et al. Phosphorylation of Thr-^{948} at the C terminus of the plasma membrane H^+-ATPase creates a binding site for the regulatory 14-3-3 protein. Plant Cell. 1999; 11: 2379–2391. [PubMed: 10590165]
25. Baunsgaard L, Fuglsang AT, Jahn T, Korthout H, Palmgren M. The 14-3-3 proteins associate with the plant plasma membrane H^+-ATPase to generate a fusicoccin binding complex and a fusicoccin responsive system. Plant J. 1998; 13: 661–671. [PubMed: 9681008]
26. Olsson A, Svennelid F, Ek B, Sommarin M, Larsson C. A phosphothreonine residue at the C-terminal end of the plasma membrane H^+-ATPase is protected by fusicoccin-induced 14–3–3 binding. Plant Phys. 1998; 118: 551–555.
27. Haruta M, et al. Molecular characterization of mutant Arabidopsis plants with reduced plasma membrane proton pump activity. J Biol Chem. 2010; 285: 17918–17929. [PubMed: 20348108]
28. Carbonell A, et al. New generation of artificial microRNA and synthetic trans-acting small interfering RNA vectors for efficient gene silencing in Arabidopsis. Plant Phys. 2014; 165: 15–29.

29. Zhang Y, Xiao G, Wang X, Zhang X, Friml J. Evolution of fast root gravitropism in seed plants. Nat Commun. 2019; 10: 1–10. [PubMed: 30602773]

30. Yamauchi S, et al. The plasma membrane H^+-ATPase AHA1 plays a major role in stomatal opening in response to blue light. Plant Phys. 2016; 171: 2731–2743.

31. Gallei M, Luschnig C, Friml J. Auxin signalling in growth: Schrödinger's cat out of the bag. Curr Opin Plant Biol. 2020; 53: 43–49. [PubMed: 31760231]

32. Kinoshita T, Shimazaki K-I. Analysis of the phosphorylation level in guard-cell plasma membrane H^+-ATPase in response to fusicoccin. Plant Cell Physiol. 2001; 42: 424–432. [PubMed: 11333314]

33. Dindas J, et al. AUX1-mediated root hair auxin influx governs $SCF^{TIR1/AFB}$-type Ca^{2+} signaling. Nat Commun. 2018; 9: 1–10. [PubMed: 29317637]

34. Yang Y, Hammes UZ, Taylor CG, Schachtman DP, Nielsen E. High-affinity auxin transport by the AUX1 influx carrier protein. Curr Biol. 2006; 16: 1123–1127. [PubMed: 16677815]

35. Hayashi, K-i; , et al. Rational design of an auxin antagonist of the SCFTIR1 auxin receptor complex. ACS Chem Biol. 2012; 7: 590–598. [PubMed: 22234040]

36. Dai N, Wang W, Patterson SE, Bleecker AB. The TMK subfamily of receptor-like kinases in Arabidopsis display an essential role in growth and a reduced sensitivity to auxin. PloS One. 2013; 8 e60990 [PubMed: 23613767]

1. Komaki S, et al. Nuclear-localized subtype of end-binding 1 protein regulates spindle organization in Arabidopsis. J Cell Sci. 2010; 123: 451–459. [PubMed: 20067996]

2. Marc J, et al. A GFP–MAP4 reporter gene for visualizing cortical microtubule rearrangements in living epidermal cells. Plant Cell. 1998; 10: 1927–1939. [PubMed: 9811799]

3. Robert S, et al. Endosidin1 defines a compartment involved in endocytosis of the brassinosteroid receptor BRI1 and the auxin transporters PIN2 and AUX1. PNAS. 2008; 105: 8464–8469. [PubMed: 18550817]

4. Moreno-Risueno MA, et al. Oscillating gene expression determines competence for periodic Arabidopsis root branching. Science. 2010; 329: 1306–11. [PubMed: 20829477]

5. Martinière A, et al. Uncovering pH at both sides of the root plasma membrane interface using non-invasive imaging. PNAS. 2018; 115: 6488–6493. [PubMed: 29866831]

6. Dharmasiri N, et al. Plant development is regulated by a family of auxin receptor F box proteins. Dev Cell. 2005; 9: 109–119. [PubMed: 15992545]

7. Uchida N, et al. Chemical hijacking of auxin signaling with an engineered auxin–TIR1 pair. Nat Chem Biol. 2018; 14: 299. [PubMed: 29355850]

8. Bennett MJ, et al. *Arabidopsis AUX1* gene: a permease-like regulator of root gravitropism. Science. 1996; 273: 948–950. [PubMed: 8688077]

9. Swarup R, et al. Structure-function analysis of the presumptive Arabidopsis auxin permease *AUX1* . Plant Cell. 2004; 16: 3069–3083. [PubMed: 15486104]

10. Wang R, et al. HSP90 regulates temperature-dependent seedling growth in Arabidopsis by stabilizing the auxin co-receptor F-box protein TIR1. Nat Commun. 2016; 7: 1–11.

11. Rast-Somssich MI, et al. The Arabidopsis *JAGGED LATERAL ORGANS (JLO)* gene sensitizes plants to auxin. J Exp Bot. 2017; 68: 2741–2755. [PubMed: 28472464]

12. Haruta M, et al. Molecular characterization of mutant Arabidopsis plants with reduced plasma membrane proton pump activity. J Biol Chem. 2010; 285: 17918–17929. [PubMed: 20348108]

13. Yamauchi S, et al. The plasma membrane H^+-ATPase AHA1 plays a major role in stomatal opening in response to blue light. Plant Phys. 2016; 171: 2731–2743.

14. Carbonell A, et al. New generation of artificial microRNA and synthetic trans-acting small interfering RNA vectors for efficient gene silencing in Arabidopsis. Plant Phys. 2014; 165: 15–29.

15. Karimi M, Bleys A, Vanderhaeghen R, Hilson P. Building blocks for plant gene assembly. Plant Phys. 2007; 145: 1183–1191.

16. Marquès-Bueno MM, et al. A versatile multisite gateway-compatible promoter and transgenic line collection for cell type-specific functional genomics in Arabidopsis. Plant J. 2016; 85: 320–333. [PubMed: 26662936]

17. Fuglsang AT, et al. Receptor kinase-mediated control of primary active proton pumping at the plasma membrane. Plant J. 2014; 80: 951–964. [PubMed: 25267325]

18. Dai N, Wang W, Patterson SE, Bleecker AB. The TMK subfamily of receptor-like kinases in Arabidopsis display an essential role in growth and a reduced sensitivity to auxin. PloS One. 2013; 8 e60990 [PubMed: 23613767]
19. Wang Q, et al. A phosphorylation-based switch controls *TAA1*-mediated auxin biosynthesis in plants. Nat Commun. 2020; 11: 1–10. [PubMed: 31911652]
20. Cao M, et al. TMK1-mediated auxin signalling regulates differential growth of the apical hook. Nature. 2019; 568: 240. [PubMed: 30944466]
21. Lee J, et al. Type III secretion and effectors shape the survival and growth pattern of *Pseudomonas syringae* on leaf surfaces. Plant Phys. 2012; 158: 1803–1818.
22. Fendrych M, et al. Rapid and reversible root growth inhibition by TIR1 auxin signalling. Nat Plants. 2018; 4: 453. [PubMed: 29942048]
23. Li L, Krens SG, Fendrych M, Friml J. Real-time analysis of auxin response, cell wall pH and elongation in Arabidopsis thaliana hypocotyls. Bio Protoc. 2018; 8
24. Von Wangenheim D, et al. Live tracking of moving samples in confocal microscopy for vertically grown roots. Elife. 2017; 6 e26792 [PubMed: 28628006]
25. Barbez E, Dünser K, Gaidora A, Lendl T, Busch W. Auxin steers root cell expansion via apoplastic pH regulation in *Arabidopsis thaliana* . PNAS. 2017; 114: E4884–E4893. [PubMed: 28559333]
26. Boudaoud A, et al. FibrilTool, an ImageJ plug-in to quantify fibrillar structures in raw microscopy images. Nat Protoc. 2014; 9: 457–463. [PubMed: 24481272]
27. Adamowski M, Li L, Friml J. Reorientation of cortical microtubule arrays in the hypocotyl of Arabidopsis thaliana is induced by the cell growth process and independent of auxin signaling. Int J Mol Sci. 2019; 20: 3337.
28. Narasimhan M, et al. Systematic analysis of specific and nonspecific auxin effects on endocytosis and trafficking. Plant Phys.
29. Shabala SN, Newman IA, Morris J. Oscillations in H^+ and Ca^{2+} ion fluxes around the elongation region of corn roots and effects of external pH. Plant Phys. 1997; 113: 111–118.
30. De Rybel B, et al. A bHLH complex controls embryonic vascular tissue establishment and indeterminate growth in Arabidopsis. Dev Cell. 2013; 24: 426–437. [PubMed: 23415953]
31. Wendrich, JR, Boeren, S, Möller, BK, Weijers, D, De Rybel, B. Plant Hormones. Springer; 2017. 147–158.
32. Nikonorova N, et al. Early mannitol-triggered changes in the Arabidopsis leaf (phospho)proteome reveal growth regulators. J Exp Bot. 2018; 69: 4591–4607. [PubMed: 30010984]
33. Hayashi Y, et al. Biochemical characterization of in vitro phosphorylation and dephosphorylation of the plasma membrane H^+-ATPase. Plant Cell Physiol. 2010; 51: 1186–1196. [PubMed: 20516032]
34. Inoue, S-i; Takahashi, K; Okumura-Noda, H; Kinoshita, T. Auxin influx carrier AUX1 confers acid resistance for Arabidopsis root elongation through the regulation of plasma membrane H^+-ATPase. Plant Cell Physiol. 2016; 57: 2194–2201. [PubMed: 27503216]
35. Spartz AK, et al. SAUR inhibition of PP2C-D phosphatases activates plasma membrane H^+-ATPases to promote cell expansion in Arabidopsis. Plant Cell. 2014; 26: 2129–2142. [PubMed: 24858935]
36. Walter M, et al. Visualization of protein interactions in living plant cells using bimolecular fluorescence complementation. Plant J. 2004; 40: 428–438. [PubMed: 15469500]
37. Leuzinger K, et al. Efficient agroinfiltration of plants for high-level transient expression of recombinant proteins. J Vis Exp. 2013; 77 50521
38. Czechowski T, Stitt M, Altmann T, Udvardi MK, Scheible W-R. Genome-wide identification and testing of superior reference genes for transcript normalization in Arabidopsis. Plant Phys. 2005; 139: 5–17.

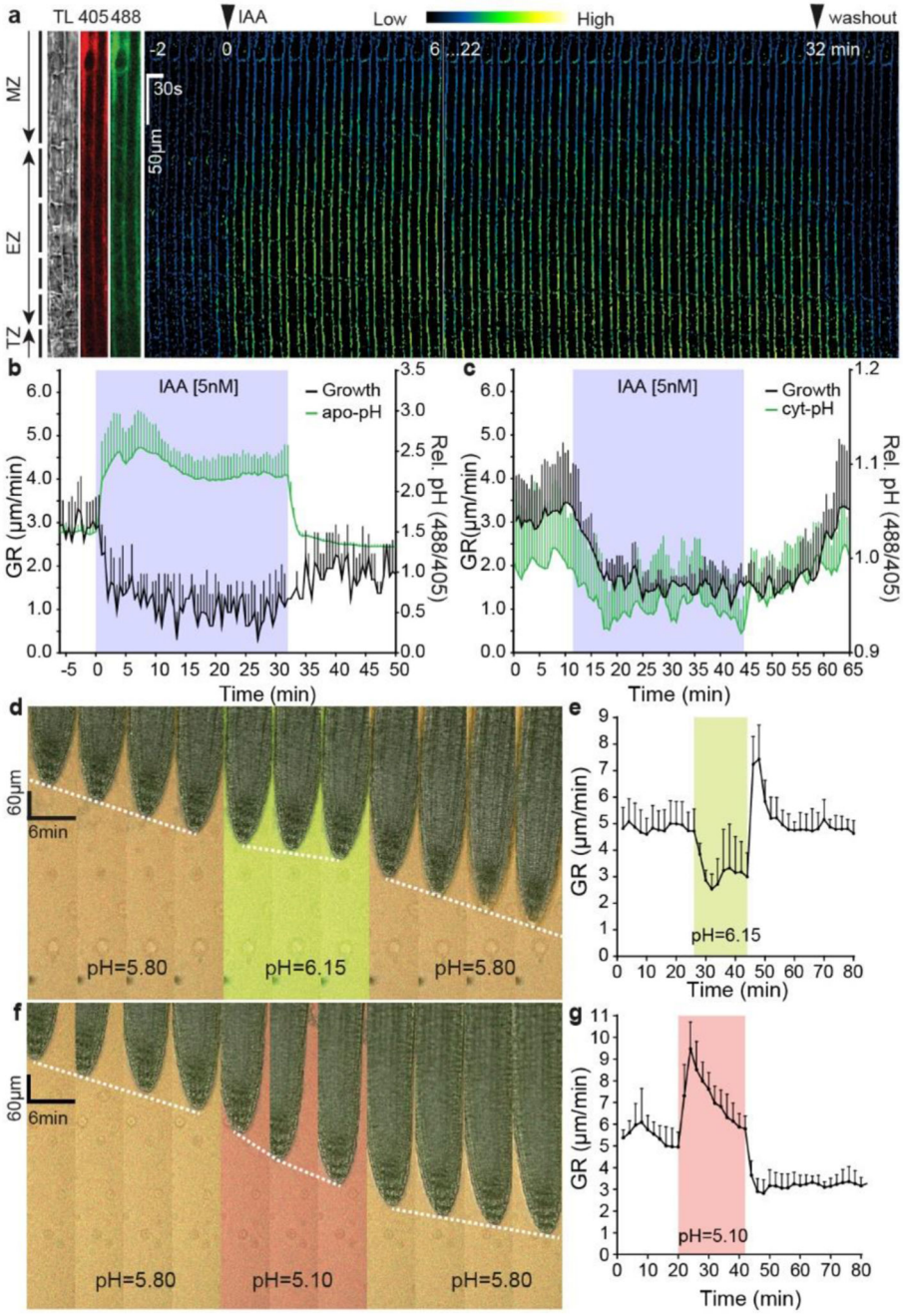

Figure 1. Auxin rapidly inhibits root growth by alkalinising the apoplast

a, Time lapse of the apoplastic pH response in root tip epidermal cells to 5 nM IAA treatment followed by auxin washout (basal auxin-free medium) in vRootchip. pH was monitored in the same region of interest (ROI) for 36 minutes by the ratiomeric HPTS dye. The ratio-image represents the ratio of excitation 488 nm and 405 nm. ROI covers maturation zone (MZ), elongation zone (EZ) and transition zone (TZ). TL is transmitted light image.

b, Quantitative analysis of the auxin-induced apoplast alkalinisation in the EZ reported by HPTS dye and corresponding inhibition and recovery of root tip growth rate (GR) following 5 nM IAA and washout as in (**a**). Means of 4 roots + SD.

c, Quantitative analysis of the auxin-induced cytoplasm acidification in the EZ, visualized by the PM-cyto reporter and the corresponding inhibition and recovery of GR upon 5 nM IAA treatment and washout in vRootchip. Means of 3 roots +SD.

d-g, Time-lapse of root growth response to a pulse of alkaline (pH 6.15) (**d**) or acidic medium (pH 5.10) (**f**). The slope of the white dotted line that tracks the root tip indicates the GR. Quantifications of GR in **d** (n = 8) (**e**) and **f** (n = 7) (**g**). The shaded areas represent the duration of the indicated treatments. Mean +SD.

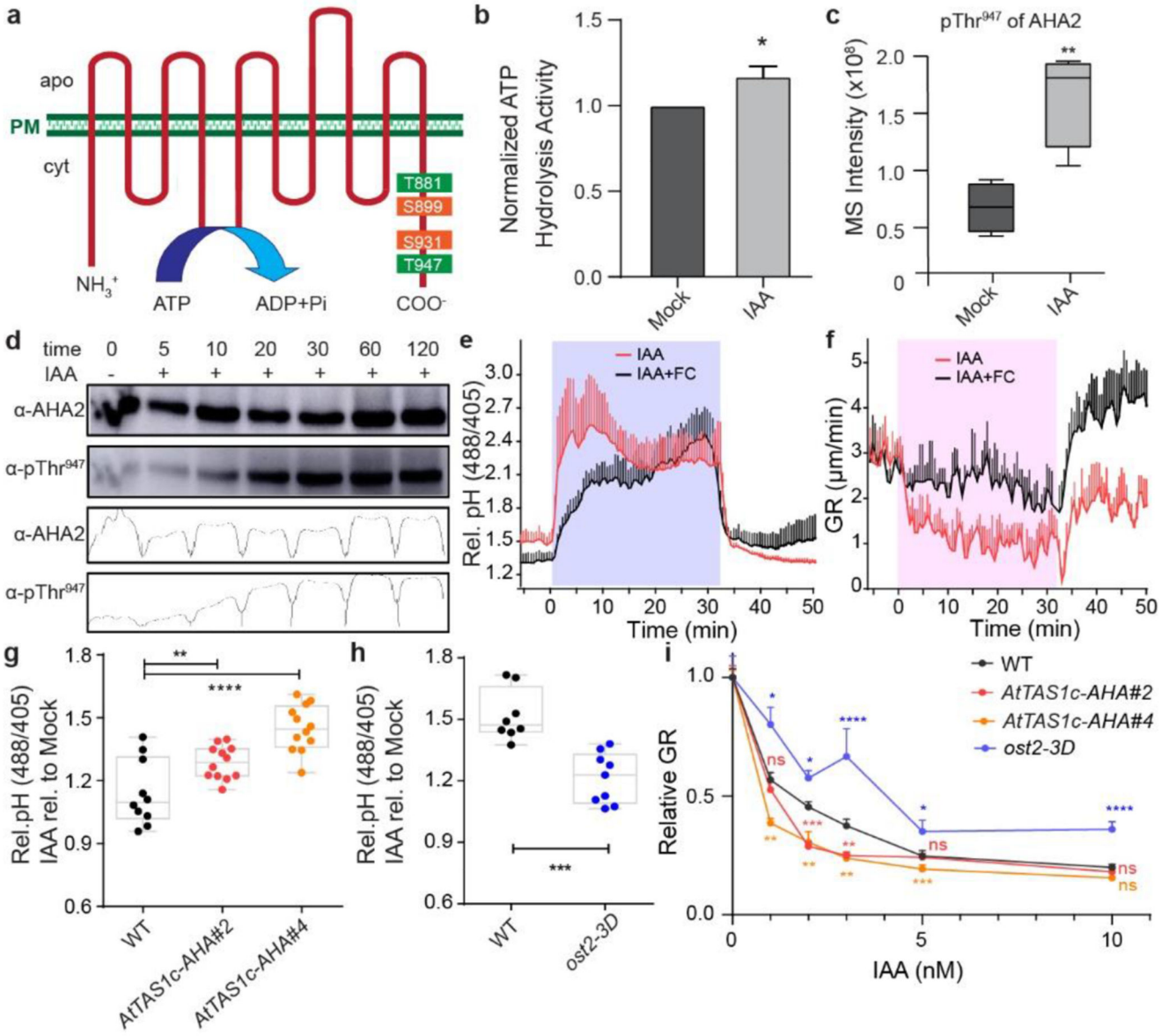

Figure 2. Auxin-triggered H^+-ATPase phosphorylation and activation counteract auxin-mediated apoplast alkalinisation and growth inhibition

a, Representation of the phospho-sites in the model of the *Arabidopsis thaliana* H^+-ATPase 2 (AHA2) identified in the phospho-proteomic analysis of auxin-treated root samples (2 minutes of 100 nM IAA). The color reflects their impact on the H^+-translocation activity (green for activation and orange for inhibition).

b, Quantification of ATP hydrolysis induction in root samples treated with 100 nM IAA for 1 hour in comparison to mock-treated roots. The IAA-treated sample was normalized by the corresponding mock-treated sample. Bars indicate means of 3 biological replicates + SD. Unpaired t-test. * $p \leq 0.05$.

Europe PMC Funders Author Manuscripts

c, Phospho-proteome detection of auxin-induced AHA2-Thr^{947} phosphorylation after 2 minutes of 100 nM IAA treatment. n= 4. Box plot depicts minimum to maximum, mean ± SD. Two-sample t-test (part of MaxQuant-Perseus analysis). **p≤0.01.

d, Time-course western blot analysis of auxin-induced Thr^{947}-phosphorylated AHA2 levels in roots treated with 10 nM IAA using AHA2 and pThr^{947}-specific antibodies. Total AHA2 protein levels were monitored in the same samples as a control. Band intensities of the different lanes are quantified by the Gels Analysis function in ImageJ.

e-f, Apoplastic pH (**e**) and root growth (**f**) analysis upon pharmacological activation of H^+-pumps by 10 μM FC and 10 nM IAA in vRootchip. Apoplastic pH was monitored using HPTS. The shaded area represents the duration of the indicated treatment. Mean of 4 roots for each treatment + SD. p≤0.0001 between IAA and IAA+FC, from 0 – 32 min (**e**), from 0 – 31 min (**f**), Two-way ANOVA.

g-h, Apoplastic pH response in two independent AHA knock-down lines (*AtTAS1c-AHA*#2 and #4) ($n > 9$) (**g**), and the *ost2-3D* gain-of-function allele ($n > 5$) (**h**) in response to 30 minutes 5 nM IAA treatment. Apoplastic pH changes are determined by the HPTS dye and IAA treatment was normalized to the corresponding mock-treatment. **p≤0.01, ***p≤0.001, ****p≤0.0001, One-way ANOVA.

i, Dose-response of auxin-induced root growth inhibition of *AtTAS1c-AHA* lines and *ost2-3D* mutants reveals hypersensitivity and resistance respectively to IAA in comparison to WT ($n > 15$) (**i**). The relative GR is calculated by the ratio of GR for each IAA concentration relative to mock-treated GR of the same genotype. *p≤0.05, **p≤0.01, ***p≤0.001, ****p≤0.0001, Welch ANOVA.

Europe PMC Funders Author Manuscripts

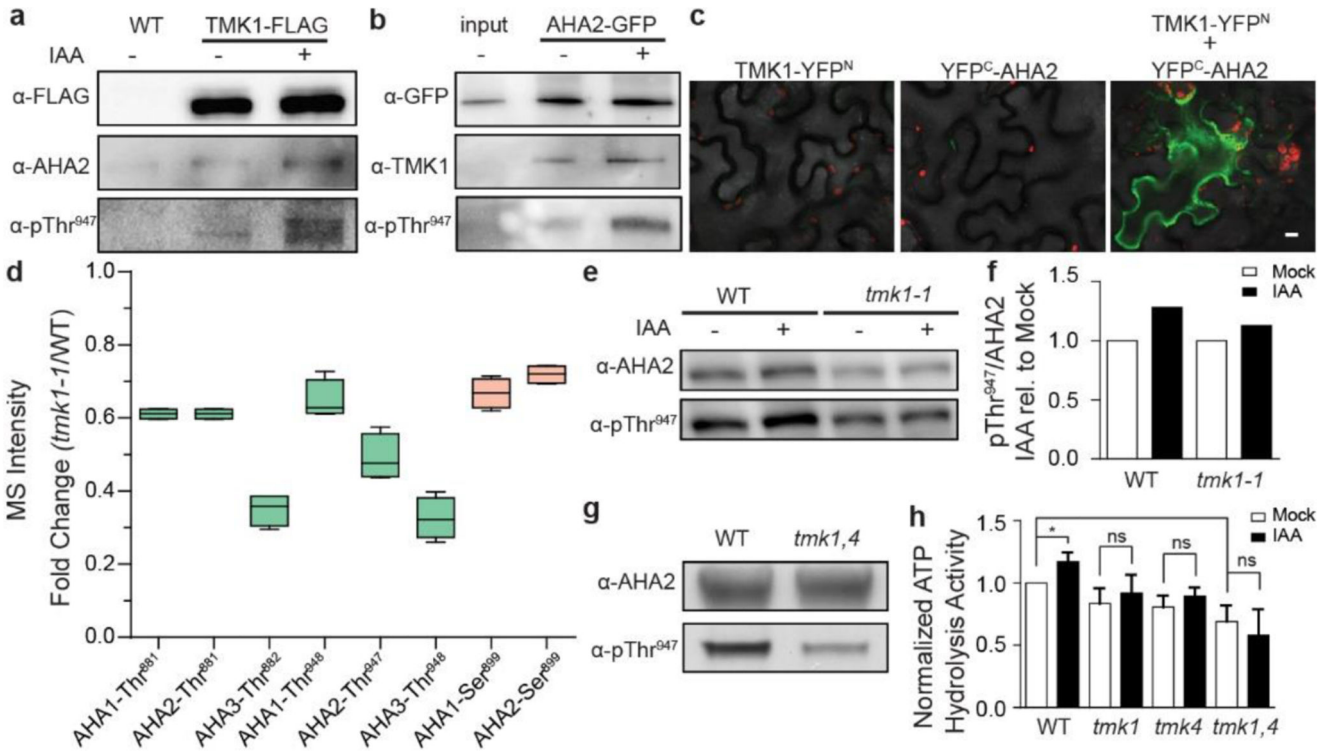

Figure 3. TMK1 directly mediates auxin-induced H^+-ATPase activation.

a, Co-immunoprecipitation (co-IP) of the *pTMK1::TMK1-FLAG* from roots mock or 100 nM IAA-treated for 30 minutes, followed by Western blot detection of AHA2 and Thr^{947}-phosphorylated AHA2. The control is the co-IP of WT (Col-0) roots.

b, Co-IP of *pAHA2::AHA2-GFP* from roots, followed by Western blot detection of TMK1 and Thr^{947}-phosphorylated AHA2 on roots mock or 100 nM IAA-treated for 30 minutes. Interaction does not depend on auxin presence, but auxin-induced phosphorylation of the interacting AHA2 was observed. As a control sample we include input of of *pAHA2::AHA2-GFP* roots.

c, Bimolecular Fluorescent Complementation (BiFC) in *Nicotiana benthamiana* leaves transiently transformed either with *TMK1-YFP^N* (*TMK1* in *pSPYNE), YFP^C-AHA2* (*AHA2* in *pSPYCE)* or both. Scale bar = 10 μm.

d, Differentially detected phospho-sites of AHAs in *tmk1-1* normalized to WT (Col-0) MS detection levels. We observe less phosphorylation on the indicated phospho-sites in AHA1, AHA2 and AHA3 in the *tmk1-1* mutant. Green indicates the sites with known activation function, while orange is used for known inhibitory function. n= 4. Box plot depicts minimum to maximum, mean ± SD. Two-sample t-test (part of MaxQuant-Perseus analysis).

e, Western blot analysis of auxin-induced AHA2 Thr^{947} phosphorylation in WT and *tmk1-1* roots treated with 100 nM IAA for 1 hour. AHA2 levels were determined as a control.

f, Quantification of the auxin effect on AHA2 phosphorylation in (**d**) by normalising the intensity ratio of $pThr^{947}$ to AHA2 in auxin-treated root samples to the same ratio in mock-treated samples of the respective genotypes.

g, Western blot detection of the AHA2 levels and its Thr^{947} phosphorylation in full seedlings shows reduced AHA2 phosphorylation in *tmk1,4* compared to WT.
h, Auxin-induced ATP hydrolysis activity is impaired in *tmk* mutants relative to WT roots (1 hour mock or 100 nM IAA treatment). The IAA-treated sample was normalized to the mock-treated WT. Means of 3 biological replicates + SD. *p≤0.05, ns p>0.05, One-way ANOVA.

Europe PMC Funders Author Manuscripts

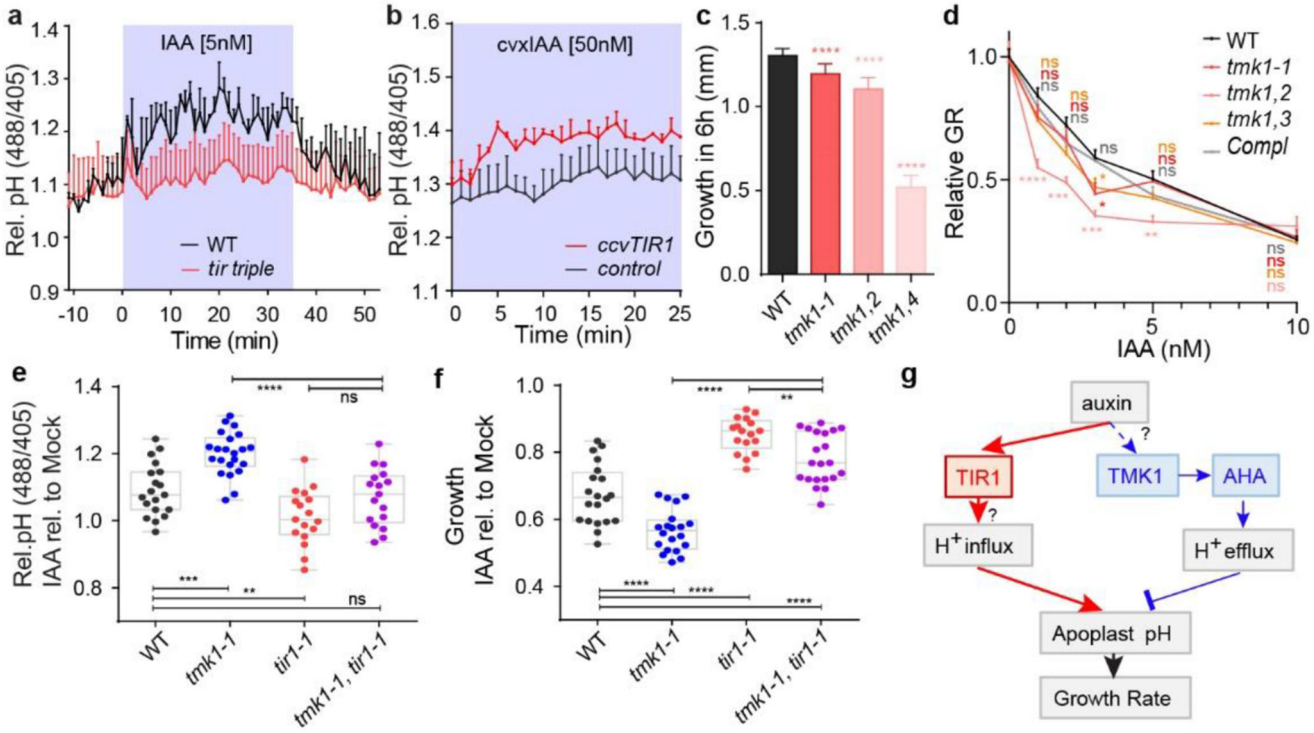

Figure 4. TIR1/AFB and TMK1 signalling converge antagonistically on apoplastic pH and growth regulation.

a, Apoplastic pH analysis by the HPTS dye shows an impaired auxin response (to 5nM IAA) in *tir triple* mutant roots (in red) compared to WT roots (in black) in vRootchip. Means of 3, 2 roots + SEM. p≤0.0001, Two-way ANOVA.

b, Apoplastic pH analysis by the HPTS dye shows apoplastic alkalinisation in *ccvTIR1* line (in red) compared to the *control* line (in black) in response to cvxIAA in vRootchip. Means of 2, 3 roots + SEM. p≤0.01, from 0 - 5 minutes, Two-way ANOVA. The shaded area represents the duration of the indicated treatment.

c, Steady-state root growth over 6 hours in *tmk1*-related mutants. n = 6 for *tmk1,4*; n > 26 for others. ****p≤0.0001, One-way ANOVA.

d, Dose-response of auxin-induced root growth inhibition of *tmk1*-related mutants relative to WT and a complemental line (*pTMK1::TMK1-FLAG* in *tmk1-1*). Relative GR is the ratio between auxin-affected growth and mock growth for the same genotype. *n* > 15. *p≤0.05, **p≤0.01, ***p≤0.001, ****p≤0.0001, Welch ANOVA.

e-f, Apoplastic pH (***e***) and root growth (***f***) measurement in *tmk1-1*, *tir1-1* and *tmk1-1,tir1-1* mutants in response to 5 nM IAA. The apoplastic pH is indicated by the HPTS emission ratio after 50 minutes treatment. The root growth is measured after 6 hours. *n* > *16* for both graphs, ns p>0.05, **p≤0.01, ***p≤0.001, ****p≤0.0001, one-way ANOVA.

g, Model for auxin-mediated root growth regulation. Auxin induces rapid H^+-influx across the PM to alkalinise the apoplast and inhibit root growth through an intracellular, non-transcriptional branch of the TIR1/AFB signalling pathway. Concomitantly, auxin through

cell surface TMK1 activates H^+-pumps (AHAs) to promote H^+-efflux to acidify apoplast and promote growth.

Europe PMC Funders Author Manuscripts